Correspondence to:

J.-B. Roustan,
jean-baptiste.roustan@polytechnique.edu

Evidence of Reflected Internal Solitary Waves in the Strait of Gibraltar

Jean-Baptiste Roustan[1,2] , **Lucie Bordois[3]**, **Jesús Garciá-Lafuente[4]**, **Franck Dumas[3]**, **Francis Auclair[5]** , and **Xavier Carton[1]**

[1]Laboratoire d'Océanographie Physique et Spatiale (LOPS), Univ Brest, CNRS, Ifremer, IRD, IUEM, Plouzané, France, [2]Ministère des Armées, Direction Générale de l'Armement, Paris, France, [3]Service Hydrographique et Océanographique de la Marine (SHOM), Brest, France, [4]Physical Oceanography Group, Department of Applied Physics II, University of Málaga, Málaga, Spain, [5]Laboratoire d'Aérologie (LA), Toulouse, France

Abstract Large-amplitude internal solitary waves (ISWs) propagating eastward toward the Alboran Sea have long been known in the Strait of Gibraltar. New in-situ data and satellite images evidence northwestward propagating ISWs. These waves are probably the reflection of the well-known eastward propagating wave along the Moroccan shelf. A simple 2D-vertical section, run with the compressible non-hydrostatic Coastal and Regional Ocean COmmunity model, illustrates that the Moroccan slope is conducive to reflection of incident solitary waves of amplitude observed in the Strait of Gibraltar. A clear signature of these waves in the Tarifa high-frequency sea level oscillations is depicted that paves the way to studies of the seasonality of ISWs in the Strait of Gibraltar with the long-time series of sea level at Tarifa. The polarity of the reflected waves, observed with Acoustic Doppler Current Profilers/Conductivity-Temperature-Depth array moorings, presents a slight variability possibly due to the internal tide oscillations. The reflected ISWs arrives at the mooring location in phase with the peak of the internal tide. For the strongest tide, the pynocline approaches a critical point where the polarity of the ISWs might reverse.

Plain Language Summary The Strait of Gibraltar is known as a hotspot for internal solitary waves (ISWs) generation, which propagate eastward toward the Alboran Sea. A new in-situ data set combined with satellite images reveal northwestward propagating ISWs in the Strait of Gibraltar. These waves are likely generated by the reflection of the eastward propagating waves on the Moroccan shelf as shown by simple numerical simulations. The reflected wave train, whose leading wave can be either an elevation or a depression wave, arrives at the observation site in phase with the internal tide trough (maximum sinking of the isopycnals). In strong spring tides, the interface depth approaches the critical point, which allows the possibility of change of wave-polarity, that is, depression versus elevation, thus explaining the double nature of the observed leading waves. Signatures of the reflected waves have been also identified in the high-frequency sea level oscillations at Tarifa. This study paves the way for long-term observations of ISWs in the Strait of Gibraltar.

1. Introduction

The Strait of Gibraltar (SoG hereafter) is the only connection between the Mediterranean Sea and the Atlantic Ocean. The density difference between Atlantic and Mediterranean waters, mainly due to the evaporation of the Atlantic water along its course in the Mediterranean basin, drives a baroclinic exchange in the SoG (Bryden et al., 1994; Lacombe & Richez, 1982). The cold and salty Mediterranean waters flow toward the Atlantic (Mediterranean outflow) underneath fresher and warmer Atlantic waters flowing at the surface toward the Mediterranean basin (inflow or Atlantic Jet). This baroclinic exchange creates a permanent halocline throughout the SoG where internal gravity waves of different scales can propagate.

In addition to this long-term two-way exchange, the SoG holds strong tidal currents dominated by semidiurnal constituents, particularly M2, which are notably influenced by diurnal constituents, thus causing a marked diurnal inequality of tidal currents (Candela et al., 1990; García-Lafuente et al., 1990). The pronounced topographic features of the SoG, which include sills and narrows (Figure 1), increase locally these currents and give rise to outstanding internal tides and associated high-frequency phenomena (Bryden et al., 1994; García-Lafuente et al., 2000), among which the generation of large short-period internal waves over the main topographic feature of Camarinal Sill (CS hereafter, Figure 1a) stands out (Armi & Farmer, 1988; Wesson & Gregg, 1994). Despite the baroclinic nature of the tidal dynamics, the barotropic tide, linked to the sea level oscillations, is useful to
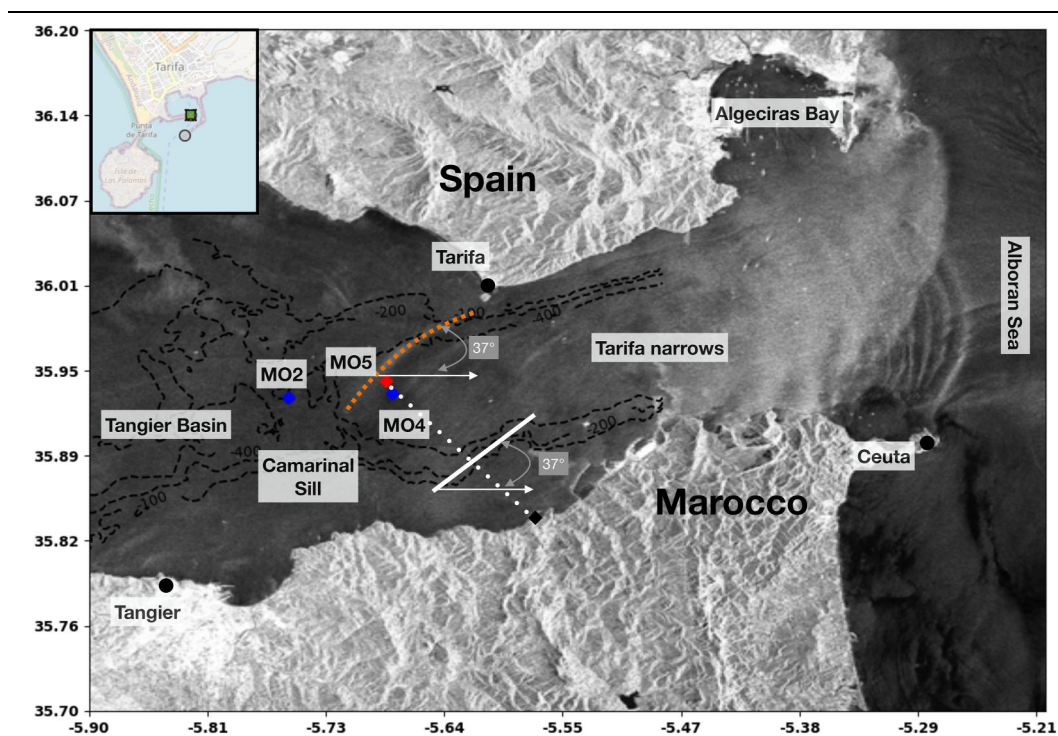
Figure 1. Map of the studied area over Sentinel-1 Synthetic Aperture Radar (SAR) image. Black dashed lines show few isobaths in the western part of the domain. Blue diamonds correspond to MO2, MO4 Acoustic Doppler Current Profilers moorings, red diamond corresponds to MO5 CT mooring. Orange dashed line shape the R-wave of the SAR image (see text). White line is the spatially averaged tangent of the isobaths along the Moroccan shelf, which is oriented 37° with respect to the east (gray text). White dotted line corresponds to the section used in the numerical approach (see Section 5). *Inset*: Zoom on Tarifa harbor, the green squared depicting the location of the tide gauge.

describe this dynamics. A barotropic tidal flow is associated to these oscillations, which heads west between low and high water (flood or west-going tide) and east from high to low water (LW) (ebb or east-going tide) because of the standing-wave pattern of the semidiurnal tide in the area (Candela et al., 1990; García-Lafuente et al., 1990, 2000). In the following, ebb and flood refer to sea level oscillations measured at Tarifa.

The combination of the tidal current with the baroclinic flow triggers high-frequency processes over CS, with sporadic hydraulic control (Armi & Farmer, 1985, 1988; Wesson & Gregg, 1994). In spring tide floods, the flow is controlled over the Sill which triggers a hydraulic jump (Armi & Farmer, 1988; Gonzalez et al., 2023; Hilt, 2022; Hilt et al., 2020; Roustan et al., 2023; Sánchez-Garrido et al., 2011; Wesson & Gregg, 1994). Since the control is tide-induced, the slackening of the tidal flood releases the hydraulic jump that propagates eastward as a bore. The highly non-linear dynamics associated with such a process gives rise to non linear internal solitary waves (ISWs) propagating toward the Mediterranean Sea (Bolado-Penagos et al., 2023; Sánchez-Garrido et al., 2008; Vlasenko et al., 2009; Ziegenbein, 1969, 1970).

The eastward propagating ISWs have been known for a long-time. The first in-situ evidence of these short internal waves were reported by Ziegenbein (1969, 1970) with mooring measurements, and later by Armi and Farmer (1988) in a more complete pioneering campaign, *The Gibraltar Experiment*. The arrival of remote sensing tools made it possible to observe the horizontal structure of these waves propagating toward the Mediterranean sea (Alpers et al., 1996; Gomez-Enri et al., 2007; Richez, 1994; Watson & Robinson, 1990). ISWs are associated with noticeable vertical currents and isopycnal displacements of typically one hundred meters (Armi & Farmer, 1988; Bolado-Penagos et al., 2023; Ziegenbein, 1969). The strong vertical current triggers convergence/divergence zones at the surface, associated with the front of the waves, which are the basis for its optical detection from satellites. The ISWs are characterized by boiling water at the surface (Bruno et al., 2002), which therefore impacts the surface roughness of the sea and has a signature on the radar measurements (Gomez-Enri et al., 2007;

Watson & Robinson, 1990). Coastal radars and Synthetic Aperture Radar (SAR) images have been widely used to analyze ISWs in the Strait of Gibraltar (Dessert et al., 2022).

So far, ISWs with different propagation directions have been observed in the SoG (Jackson & Apel, 2004). The eastward propagating ISWs are the best known and most impressive waves. They are generated by the release of the hydraulic jump at CS when the flood current slackens. Westward propagating ISWs, due to roughly symmetric processes during ebb tide (García-Lafuente et al., 2018), have been rarely reported and are generally associated to the seasonal thermocline rather than to the strong and permanent halocline (Brandt et al., 1996). Finally, Watson and Robinson (1990) reported northward ISWs propagating toward Algeciras Bay at the eastern exit of the SoG, which are known to impact the local mixing and biology of the bay (Chioua et al., 2013). The former authors hypothesize that this wave is a shock wave due to hydraulic control over a bathymetric feature east of Ceuta.

The shoaling of ISWs is known to be an important source of mixing along continental shelves of many regions (Jeans & Sherwin, 2001; Lamb, 2014; Laurent et al., 2011). This mechanism is therefore likely responsible for a significant part of the mixing along the continental shelf in the SoG (Vlasenko et al., 2009), impacting the biological production (Sánchez-Garrido & Nadal, 2022; Vázquez et al., 2009) but it has yet not been addressed (Wesson & Gregg, 1994). Exhibiting these new wave patterns represents a step forward in our understanding of SoG dynamics, and requires a more thorough description of the interaction between the ISWs and continental slope, particularly the Moroccan slope.

This paper presents evidence of a new ISW pattern in the SoG suspected to be reflected waves of the eastward propagating ISWs on the Moroccan coast. The next section presents a brief description of the in-situ observations employed in this study along with satellite images that illustrate the shape of this new ISWs. Then we describe this pattern from moorings deployed during a recent field experiment. From these data and a numerical approach, we provide clues to support the hypothesis of a wave reflection at the Moroccan shelfbreak. Two other interesting outcomes are also discussed. First, the reflected waves polarity presents some variability suspected to be due to the deepening of the interface under the effect of internal tides. Second, these internal waves leave a signature in the high-frequency sea level record of Tarifa tide gauge, which is a pioneering method of observing ISWs in coastal tide gauges in the SoG. Finally, we discuss our results and conclude.

2. Data

2.1. Satellite

Satellite images have been used for a long-time to characterize the ISWs propagating from CS toward the Alboran Sea. Both optical and radar images can detect changes in the surface roughness due to strong convergence/divergence zones associated with ISWs. Gomez-Enri et al. (2007) illustrated that Synthetic Aperture Radar (SAR in hereafter) images are useful to characterize ISWs propagating in the SoG. In the following, we use both optical and SAR images to describe singular wave patterns propagating northwestward.

The SAR images from the Sentinel-1 have been extensively analyzed from 2015 to 2023 in the area of the SoG (Figure 1). Figure 2a depicts the surface signature of ISWs, extracted from the set of inspected SAR images, which are of interest for this study and panels c–e show a selection of the best images of this set. Other images illustrate the same features and can be accessed on the Ocean data lab viewer (https://ovl.oceandatalab.com). An older false color optical image processed by ESA from the ERS2 sensor is presented in Figure 2f. The location of MO5 mooring and the Tarifa tide gauge are indicated on this image.

2.2. In-Situ

This study presents part of the data collected during the PROTEVS GIB20 field experiment performed during October 2020 in the SoG on the French R/V L'Atalante. In this paper, we analyze data from 3 moorings deployed over and east of CS during this campaign: 2 Acoustic Doppler Current Profilers (ADCP) at MO2 and MO4 and an array of Conductivity-Temperature-Depth (CTD) probes at MO5 (Figure 1). The ADCPs recorded almost a fortnightly cycle from 8 to 17 October 2020. The CTD array recorded a bit longer, although only the ADCP periods have been analyzed. The CT probes are equipped with pressure sensors to correct the current-induced sinking of the instrument during the strong spring tidal flows. Density profiles in this work are reconstructed from the interpolation of C-T measurements at fixed depth.
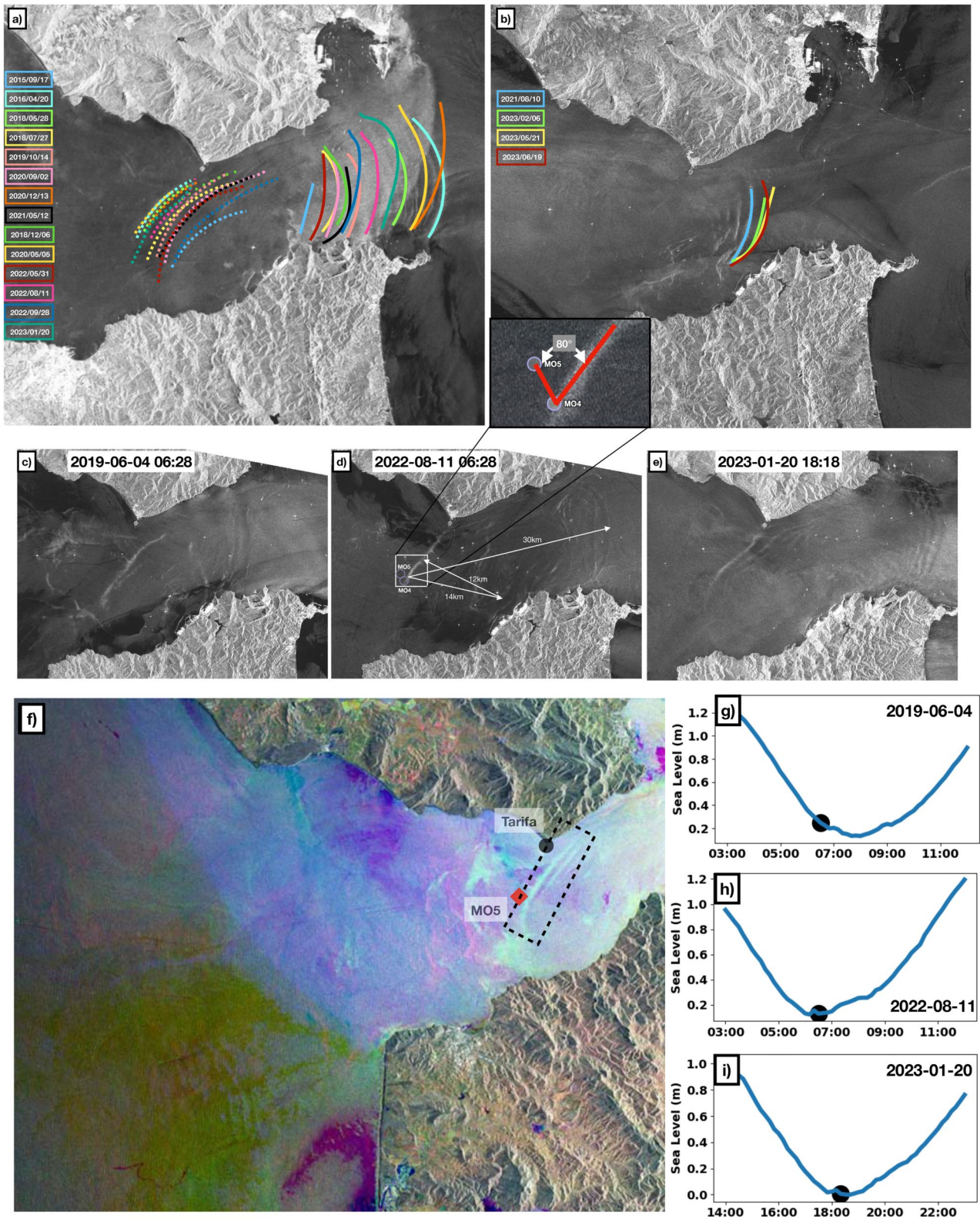
Figure 2.

MO2 is equipped with ADCP CONTINENTAL 190 kHz fixed on cage at the bottom, with 30-s sampling of 4 m thick bins, ranging from 4 m over the bottom to 36 m below the surface. This mooring is used as the reference for tidal barotropic flows as it is placed over CS where the internal bore is formed and released. The barotropic current is computed as the vertically-averaged current filtered with a 1 hr running-average. MO4 is equipped with a 75 kHz ADCP sampling from 450 m (100 m above the sea floor) to 30 m below the surface. It provides data in 8 m thick bins every minute. Finally the CTD array (MO5 mooring) is equipped with Seabird SBE37 probes sampling every 10 s spaced by 50 m.

In addition to the PROTEVS GIB20 data set, we used the Tarifa tide gauge time series of 1-min sampling interval during the whole month of October 2020 which has been retrieved from Puertos des Estado, Spain (http://opendap.puertos.es/thredds/catalog/tidegauge_tari/catalog.html).

3. Satellite Observations

Figure 2f shows a change in surface rugosity southeast of Tarifa (dashed box) that extends up to 10 km to the south. It is followed by a weaker signature to the east with a shorter extension to the south. As explained earlier, this change in rugosity is a characteristic surface signature of ISWs. Such a pattern is also visible on SAR images at different times, April 2019 (Figure 2c), August 2022 (Figure 2d) and January 2023 (Figure 2e) for example, Figures 2h and 2i show that the waves arrive in phase with the low tide (end of the ebb) in Tarifa. The wave in Figure 2c has not yet reached Tarifa as the image was taken 90 min before the low tide (Figure 2g). Both this delay and the decreasing intensity from northwest to southeast in Figure 2f suggest northwestward propagation of this internal signature.

A few images show the northwestward propagating ISWs simultaneously with the eastward propagating ones (e.g., Figures 2c–2e). In Figure 2a, we draw the front of each ISW at different dates when this situation happens on a single image. This analysis reveals a link between the northward/eastward position of the northwestward/eastward propagating ISWs. With a slight variability, attributable to the variability of barotropic current intensity that impacts differently the different waves, the farther eastward one wave propagates, the farther northward the other wave travels. This point suggests a dynamical link between these ISWs. To support this conclusion, we draw some eastward propagating ISWs before they reach the Moroccan shelf-break (Figure 2b). It highlights that the waves propagates southeastward in their southern part increasing the possible interaction with the Moroccan shelf-break.

The illustrated pattern resembles a reflected ISW propagating from the Moroccan to the Spanish coasts. Interestingly, it appears at all seasons, also in November, December and in January (Figure 2) when the seasonal thermocline is certainly absent, suggesting that this feature is linked to the halocline between the Atlantic and Mediterranean waters. This point also excludes meteorological forcing for such a wave. A last point to be mentioned, is that the wave front intercepts Tarifa at almost the same time as MO4/MO5 moorings (Figure 2g). In the following, we report evidence for the existence of such internal waves with in-situ data, and argue that they appear in the sea level high-frequency variations at Tarifa tide gauge. Finally, we argue that reflection is a possible mechanism to explain this pattern with a simple numerical approach. As far as we know, such a pattern has not been reported before either in satellite images or by in-situ observations. The results of the model run by Hilt (2022) show a reflected-like pattern in spring tides (personal communications).

4. In-Situ Observations

4.1. Moorings Analysis

Moorings MO4/MO5 were deployed east of CS with a little distance apart during the PROTEVS GIB20 experiment, to assess properties of wave propagation. We focus on the spring tide period between 13 and 17

Figure 2. (a) Synthetic Aperture Radar (SAR) image of the SoG superimposed with shape of northwestward propagating internal solitary waves (ISWs) (dashed colored lines) and eastward propagating ISWs (full colored lines) retrieved from the clearest SAR Sentinel-I images of the 2015–2023 period showing both waves (see legend on the left). (b) SAR image of the SoG superimposed with shape of eastward propagating ISWs before they reach the Moroccan shelf-break. *Inset*: Zoom on the white box of panel (d). (c–e) SAR images from Sentinel-1 at different dates (downloaded from Ocean Data Lab platform). The times of the SAR images correspond to 90, 30, and 10 min before low water (end of the ebb) at Tarifa. (f) False color ESA-ESRIN satellite image of the SoG. Locations of Tarifa and MO5 mooring are reported. The dashed box frames the discussed feature (see text). (g–i) Recorded sea level at Tarifa with the black dot showing the time of corresponding satellite image (c–e respectively).
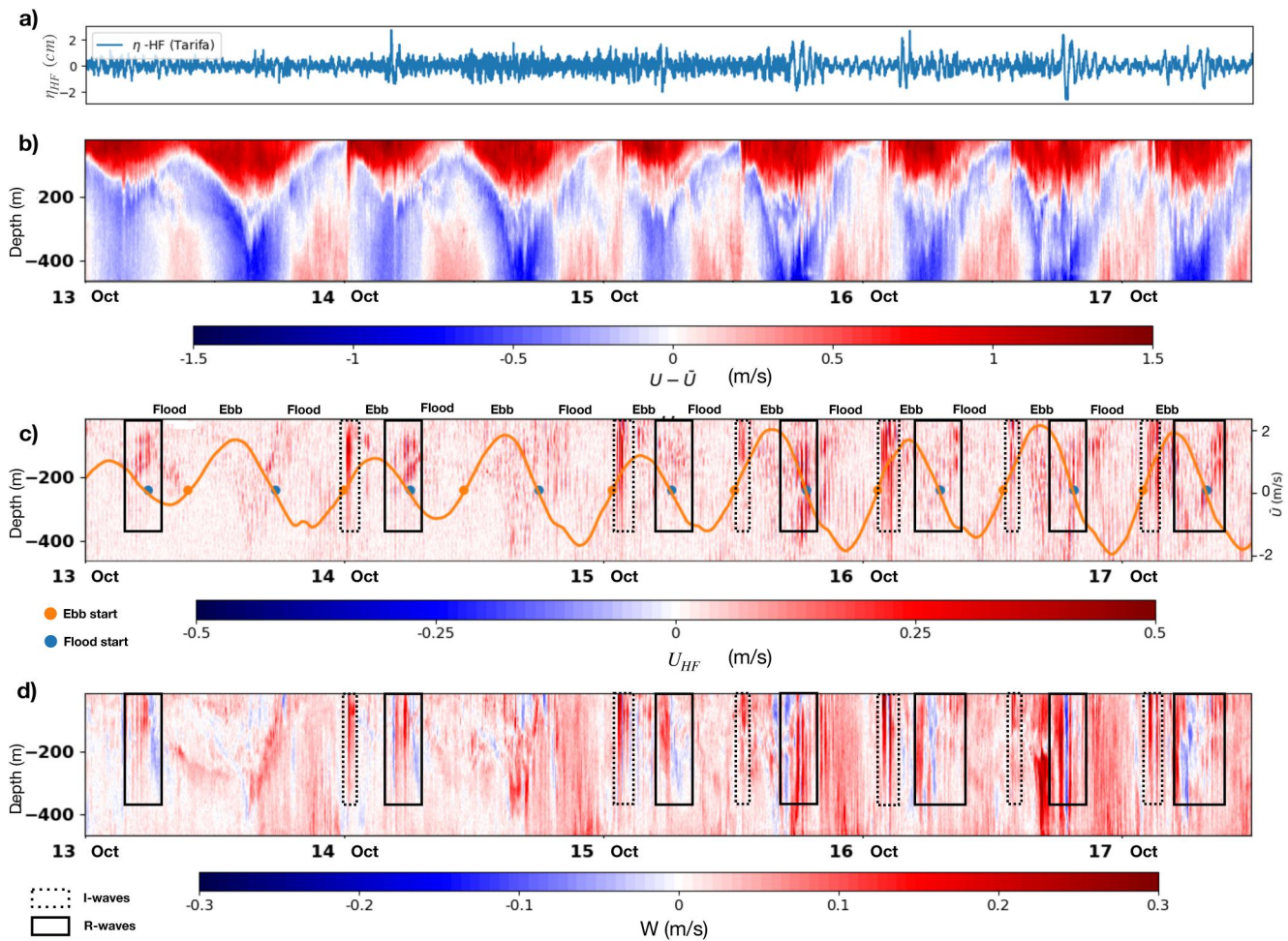
Figure 3. Current moorings and Tarifa sea level data during spring tides (13th midnight to 17th midday of October 2020). The *x*-axis labels correspond to days of October at midnight. (a) High pass (1cph 3 order Butterworth filter) sea level at Tarifa (blue curve). (b) Baroclinic zonal velocity at MO4 (computed as total current minus local barotropic current low pass filtered at 1cph). (c) High-frequency zonal velocity at MO4. A Butterworth eighth order filter at 1cph is used. Flood and Ebb periods are indicated at the top of the panel between blue/orange half-dots. The superimposed orange curve corresponds to the barotropic zonal current at MO2 (RHS of *y*-axis) (d) Vertical velocity at MO4. Thick black boxes highlight the discussed northwestward internal solitary waves (ISWs) (R-waves), thin dashed boxes indicate the well-known eastward propagating ISWs (I-waves).

October 2020. Baroclinic zonal velocity (estimated as $U(z) - \bar{U}$ with overbar variable, $\bar{U}$, for the depth-averaged velocity), high-frequency zonal velocity (eighth order Butterworth band-pass filter between 1cph and 6cph) and the vertical velocity during the whole period are presented in Figure 3. The high pass filtered (at 1 hr with third order Butterworth filter) sea level at Tarifa is plotted in the upper panel. At the start of almost each ebb, a packet of short eastward propagating ISWs (I-waves hereafter) is observed (dashed boxes in Figures 3c and 3d) followed by another signature of high-frequency variability of both the zonal and vertical velocity (black boxes in Figures 3c and 3d). These secondary patterns, denoted as R-waves in the following, appear at the end of the ebb, which excludes a generation from the released bore at CS. Indeed, the bore is known to be generated near the end of the flood, when the westward zonal current falls below 1 m/s (Vázquez et al., 2008); it propagates at a typical speed of 2 m/s (Sánchez-Garrido et al., 2008). Therefore, the eastward ISW cannot reach MO4, 5 km east of CS, later than 2 hr after the beginning of ebb tide. R-waves are suspected to correspond to the northwestward propagating wave observed on the SARs images, as both features are observed at the end of the ebb tide.

This analysis shows that the R-waves cannot be the signature of the well-known ISWs generated at CS by the end of the flood tide, which correspond to the I-waves. Even more, the repetitiveness of the R-waves after each observation of I-wave suggests a link between both features. A careful inspection of the arrival time of the R-waves shows that they arrive at MO4 at the peak of the internal ebb tide, when the interface between Atlantic
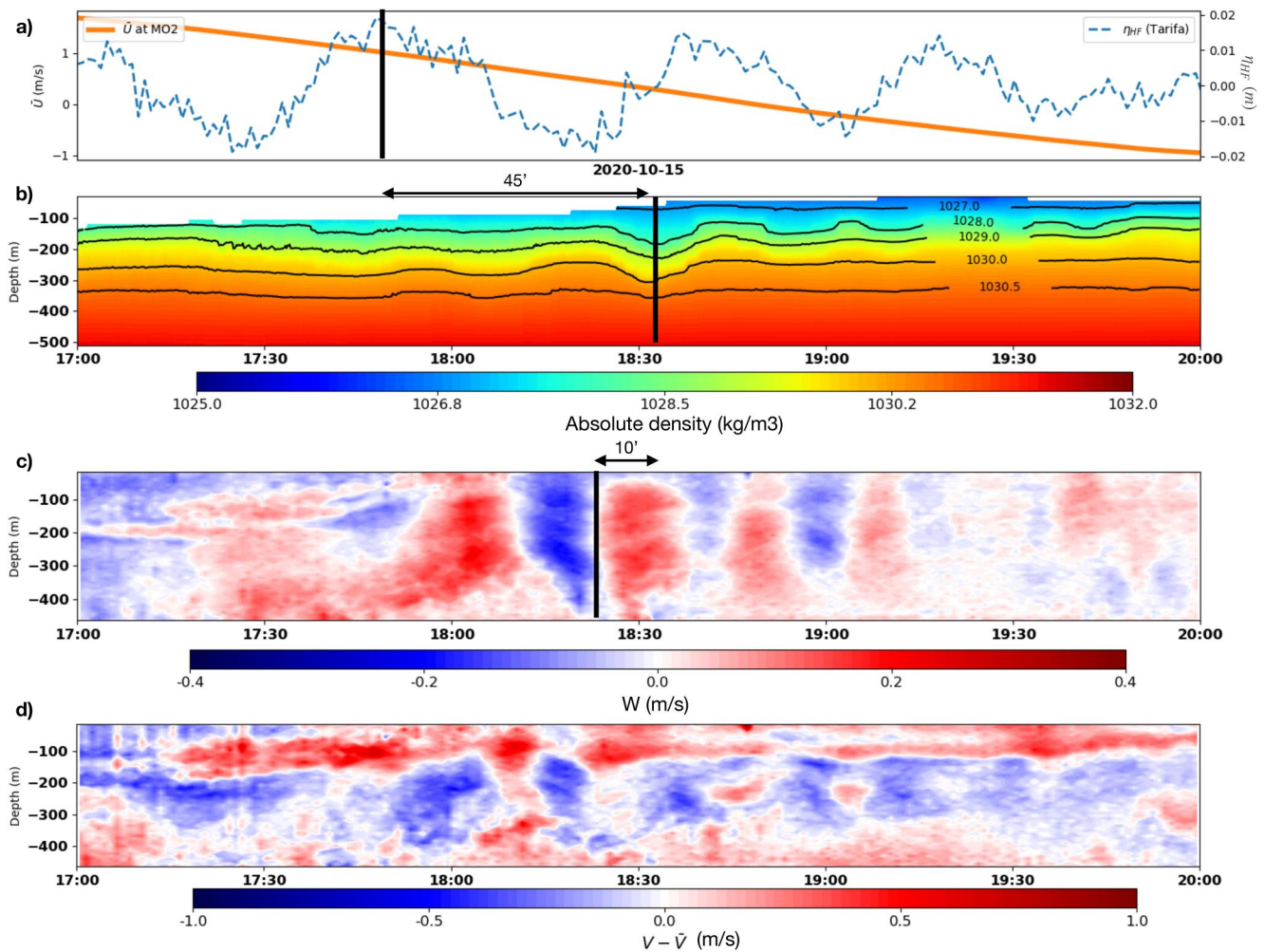
Figure 4. Zoom on one typical northwestward propagating internal solitary wave (R-wave) packet (from 17:00 to 20:00 the 15 October). (a) Barotropic zonal current at MO2 (blue curve) and high pass (1cph 4 order Butterworth filter) sea level at Tarifa (blue dashed curve). (b) Absolute density at MO5. (c) Vertical velocity at MO4. (d) Meridional baroclinic velocity at MO4, computed as the total meridional velocity minus the vertical averaged. Black vertical lines and arrows are hints for phase shift discussion (see text).

and Mediterranean waters is the deepest as suggested by the baroclinic velocity structure (see Figure 3b). The repeated phasing between these R-waves and the I-waves supports the idea of a tidally locked phenomenon.

The last point concerns the observation of the high-frequency oscillations of the sea level at Tarifa (Figure 3a). Superimposed to the background noise, we clearly distinguish spikes (of about 2 cm) which occur in phase with the R-waves.

To illustrate that the recurrent patterns of R-waves in the boxes of Figures 3c and 3d correspond to northwestward propagating ISWs we zoom on the 15 October afternoon (Figure 4). The two moorings, separated by 1.1 km, evidence a wave pattern propagating northwestward. The joint analysis of hydrological (MO5) and current (MO4) signatures presented in Figures 4b and 4c highlights a 10 ± 1 min shift between the observed signal at MO4 and MO5. Figure 4b shows a trough of the isopycnals at 18:35 which must necessarily be achieved at the end of the period of negative vertical velocity. This situates the arrival of the wave at MO4, 10 min earlier. Thus, the wave travels from MO4 to MO5, that is, northwestward. The baroclinic meridional velocity of this R-wave, confirms the northward direction of this signal. Indeed, a positive meridional current of the wave is observed in the upper layer when the depression R-wave passes at MO4 (Figure 4d), which corresponds to the expected signal of an ISW whose front has a northward propagating component (Kurkina et al., 2018; Shroyer et al., 2009). We can estimate the local phase speed of the wave, which covers 1.1 km in 10 ± 1 min, at 1.82 ± 0.15 m/s. This

computation takes into account the angle between the wave front and the moorings orientation which is about 80° (see inset in Figure 2b). The typical time scale of the depression wave is around 30 min, providing a wavelength of 3,240 m, larger than the one of I-waves whose typical wavelength is less than 1 km (Armi & Farmer, 1988; Bolado-Penagos et al., 2023; Wesson & Gregg, 1994). The amplitude of the trough at the 1,030 kg/m³ pycnocline is about 65 m (Figure 4b).

Another evidence that the signatures at MO4 and MO5 are originated by the same wave, comes from the analytical computation of the phase speed, c, based on a simple two layers Korteveg-de Vries (KdV) model (Gerkema & Zimmerman, 2008):

$$c = c_0 \left(1 + \frac{1}{2}a\frac{h_1 - h_2}{h_1 h_2}\right) \tag{1}$$

where $c_0 = \sqrt{g'\frac{h_1 h_2}{h_1 + h_2}}$ is the linear phase speed, computed as with g' the reduced gravity $g\frac{\rho_2 - \rho_1}{\bar{\rho}}$, g the local gravity, ρ_i and h_i respectively the density and the thickness of i-layer, $\bar{\rho}$ the averaged density and a the amplitude of the wave. In the situation of Figure 4, the pynocline is estimated at 200 m depth (based on the 37.5 psu isohaline not shown), which gives a phase speed of 2 m/s. At the R-wave passing time the barotropic current at MO4 is about 0.2 m/s (not shown), the front incident angle ranges between 35° and 60° (Figure 2a) with the zonal direction, that gives an opposite contribution of 0.15–0.17 m/s from the tidal current. Combining both contributions, the phase speed of the R-wave should be 1.85 ± 0.2 m/s very close to the 1.82 ± 0.15 m/s estimated from the mooring observations. This analytical computation supports that we are observing the same wave at MO4 and MO5. Using the two-layer KdV equation for such large-amplitude ISWs is questionable, because of the assumption of weak nonlinearity and the blurring of the pynocline that shed doubts on the two layer model as well. However, Hilt et al. (2020) have compared the KdV theory with a fully nonlinear model, and have found a reasonable agreement. Following this previous argument between models, in this area, we use the two-layer KdV theory as a simple and convenient framework to roughly characterize the ISWs propagating in the SoG.

Sea level high-frequency oscillations at Tarifa show an elevation (of about 2 cm) starting 45 min earlier than the depression R-wave observed at MO5 (Figure 4a). This signal at Tarifa is phased with the internal waves observed at MO4/MO5, arguing for a common origin as suggested by the satellite images. Indeed, as mentioned above, the R-wave fronts observed both on SAR and optical images intercept Tarifa and our moorings slightly synchronously. This supports the assumption that the recurrent high-frequency sea level oscillations at Tarifa are the signature of the R-waves.

4.2. R-Waves Variability

The R-waves discussed in this paper are observed in spring tides whenever the I-waves are released from CS (Figure 3). Even if they are well phased with the end of the ebb, they present a large variability in their shape and polarity. Figure 5 illustrates two different patterns of these waves for different tidal cycles along with the barotropic tidal current at MO2 and the high-frequency variations of the sea level at Tarifa. In both cases, R-waves follow a group of shorter eastward ISWs (I-waves) generated by the released bore at the end of the tidal flood at CS (see at 00:15, 02:00, 14:00 in Figures 5b and 5d respectively). The variability of the I-waves is not the topic of this paper and will be discussed in a dedicated study. In the following, we describe the variability of the R-waves.

The 14 October, the first R-wave arrives at 04:45 at MO4 and a few minutes later at MO5 (Figure 5b). It is followed by other smaller internal waves in its tail. The R-wave has a typical period of 30 min which corresponds to a wavelength of 3,240 m. This computation is based on a phase speed of 1.8 m/s deduced from the distance between both moorings and the same time delay of 10 min. The last remark concerns the polarity of the wave, the vertical velocity signature clearly indicates a soliton of depression characterized by the negative followed by positive anomalies of the vertical velocity, when observing from an Eulerian point of view. The isopycnal displacement at MO5 confirms the depression-like shape.

The 16 October afternoon, the R-waves arrive between 18:15 and 19:30 at MO4 (Figure 5d). A clear depression of the isopycnal surface at MO5 is observed at 19:15 with a delay of about 10 min giving the same typical phase speed of 1.8 m/s as before. The period of the signal is around 45 min, which gives a longer wavelength of 4,860 m. The interesting point to discuss is the polarity of the wave. The vertical velocity is first positive and then changes
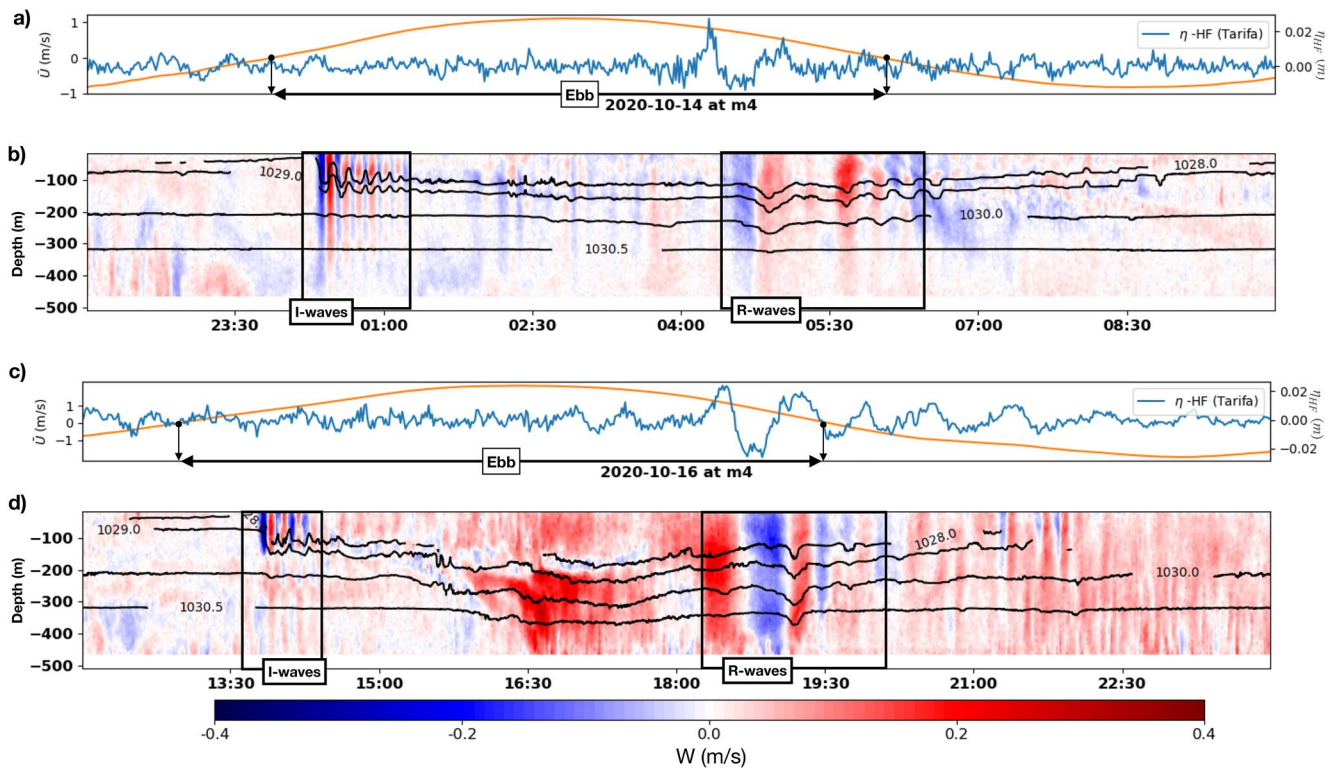
Figure 5. Barotropic current at MO2 (orange curve), high-pass sea level at Tarifa tide gauge (blue curve), vertical velocity at MO2 (red/blue shade) and isopycnals at MO5 for typical northwestward propagating internal solitary waves. (a, b) From 22:00 the 13 October to 10:00 the 14 October. (c, d) From 12:00 to 24:00 the 16 October. R-waves and I-waves are framed with black boxes.

to negative, which is a typical signature of an elevation wave. Even if the isopycnals elevation before the clear depression is less evident (MO5 at 19:00), they are rising slowly and with a slight delay to the positive vertical velocity at MO4. This observation suggests that the R-wave is not a simple depression solitary wave as the incident I-wave. It has a more complex structure which can be named a transition between depression and elevation polarity similar to a wave reaching a critical point when shoaling on a shelf.

The difference in the polarity of the two discussed R-waves raises the question of which physical process causes the observed variability. The barotropic tidal current at MO2 is twice stronger on the 16th than on the 14th. This clearly impacts the amplitude of the internal tide with a deepening of the interface (determined by the depth of maximum shear of the baroclinic current) between Atlantic and Mediterranean waters by 50 m (Figure 3). As the observed R-waves are in phase with the deepest point of the internal tide, it suggests that the amplitude of the internal tide might influence the polarity of the waves. In a two-layer framework, the KdV equation for modeling solitons provides a useful criterion to assess the polarity of the wave. The soliton is depression like as long as the interface depth is shallower than mid-depth. This theoretical approach along with the observations of the interface deepening with increasing tidal strength, supports the fact that internal tide variations might cause the variability of the polarity of the R-waves. This point will be further addressed in the discussion.

Despite the differences, both R-waves in Figures 4b and 4d have a similar pattern of associated in-phase spikes in the high-frequency oscillations of the sea level at Tarifa, supporting the fact that these waves leave a signature in the sea level at Tarifa.

4.3. Tarifa Sea Level Signature of ISWs

The previous analysis of mooring observations and high-frequency oscillations of sea level at Tarifa along with the orientation of the surface front in the satellite images (Figures 2c–2e, and 2g) suggests that the Tarifa tide-gauge could detect the R-waves. A suitable parameter to identify high-frequency oscillations is the square of the band-pass filtered sea level series. The mooring data analysis indicates wave periods between 30 and 60 min,
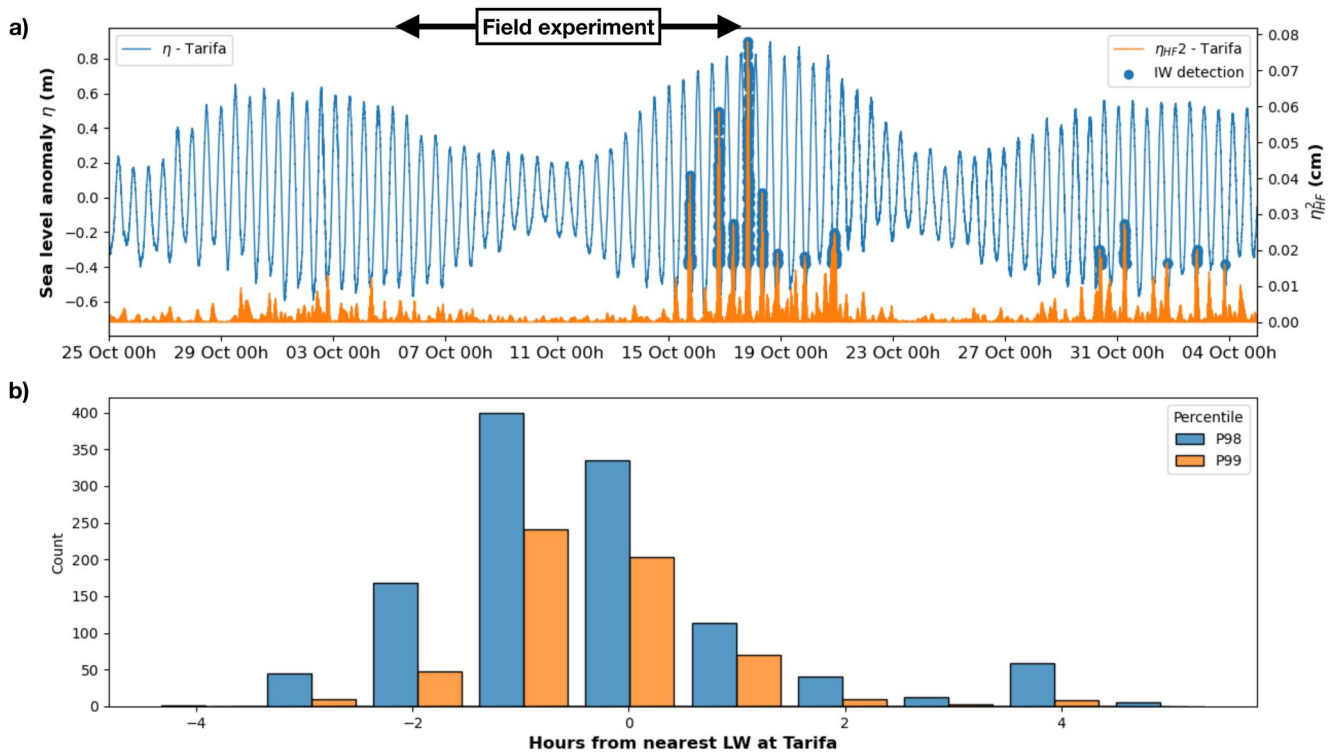
Figure 6. (a) Sea level at Tarifa tide gauge during three fortnightly cycles framing the field experiment (blue curve LHS *y*-axis). Squared band pass sea level at Tarifa (orange curve RHS *y*-axis). Peak detection over 99-percentile (blue dots). (b) Histogram of the time shift between Tarifa nearest Low Water (LW) and the P99 (blue), P98 (orange) percentile detection in the high pass squared sea level signal.

values used to build a eighth order Butterworth band-pass filter to extract the high-frequency signal. Then we define spikes as the value over a certain percentile of this signal.

Figure 6a presents the sea level at Tarifa in October 2020 and the square of this signal along with the identified spikes using the 99% percentile, considered as the signature of the R-waves. During the field experiment, spikes are well correlated with the fortnightly cycle, being present during spring tide and no spikes in neap tides. The pattern is consistent with the observations at M04/M05 moorings, which did not exhibit R-wave signatures during neap tides either. Figure 6b shows the histogram of the time shift between the spikes detection and the nearest LW at Tarifa. LW occurs at the end of the ebb cycle due to the standing-wave nature of the barotropic tide (Candela et al., 1990; García-Lafuente et al., 1990). For two detection thresholds (99% and 98% percentiles), most of the spikes fall within 2 hr around LW, in good agreement with observations, which indicates the wave arrivals by the end of the ebb tide. It strongly supports our assumption that the high-frequency sea level oscillations are a signature of the R-waves. In addition, power spectra in the high-frequency band (high pass at 1cph) for moorings and sea level data show a concentration of energy in the same period of 40–50 min, consistent with the hypothesis of a R-waves signature in the sea level oscillation at Tarifa (Figure 7). These spectra highlight that the R-waves are supported by a pycnocline located deeper than for the I-waves. Indeed, the energy spike for the I-waves (near 10 min) is notable in the zonal current at 100 m but not at 200 m (Figure 7a). The energetic spike at 8 min in the high-frequency sea level oscillation at Tarifa is attributed to the seiche phenomenon rather than to I-waves whose front shape is not suitable for a coastal detection at Tarifa (the tide gauge is on the eastern side of the tip of Tarifa inset Figure 1). In addition, Delgado et al. (2011) showed that the resonant period of the Tarifa harbor falls between 7 and 8 min, which corresponds to the peak labeled "seiche" in the high-frequency sea level oscillation spectrum in Figure 7b.

The sea level analysis was extended to three fortnightly cycles framing the in-situ measurements to get insights on the variability over a longer period. Few spikes were detected during the last spring period of the month and none during the first one. These two spring tides were notably weaker than the one of the middle of the month, when the field experiment was carried out, because of the monthly modulation associated to the ellipticity of the moon orbit (N2—larger lunar elliptic—tidal constituent). This modulation is likely the reason of the asymmetry in Figure 6a.
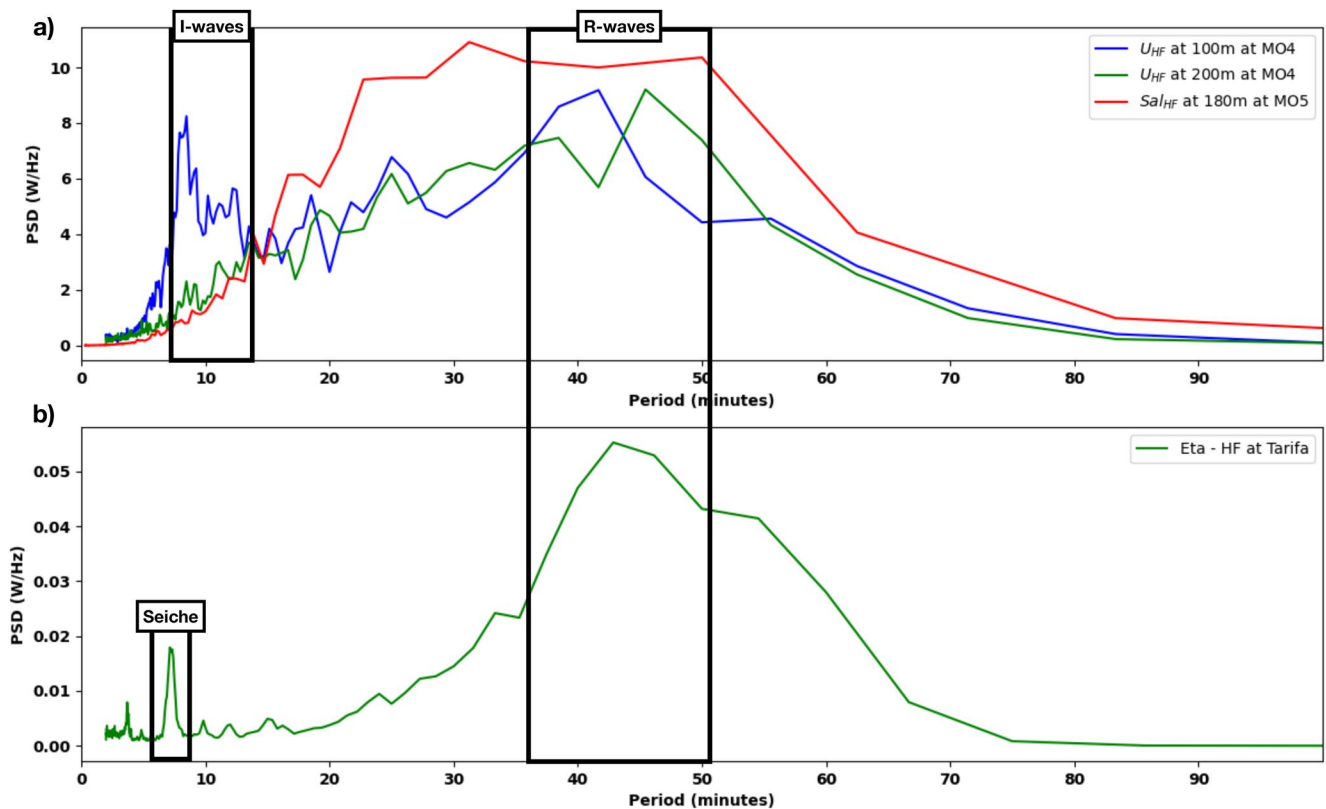
Figure 7. Density power spectra for 1cph high pass signals of (a) Zonal current at 100 m depth (blue curve), 200 m depth (green curve) and Salinity at 180 m (red curve); (b) sea level oscillation at Tarifa.

However, the high-frequency series show peaks phase-locked with sea level LWs during these weaker spring tides as well. This suggests that the R-waves are present at almost every spring-tide ebb. Or, at least, every time the I-waves are released at CS. Their appearance is favored by the strength of the tide as illustrated by the spring tide of mid-October in Figure 6a.

5. Numerical Approach

5.1. Set Up

In order to clarify the physical process behind the observed R-waves, we have implemented a 2D-vertical numerical approach which will be more focused than a 3D model. We resolve the full Navier-Stokes equations along a 2D vertical section with a realistic bathymetry from MO5 mooring to the Moroccan coast (white dotted line Figure 1). This approach aims to illustrate if ISWs with amplitudes typical of those of I-waves in the SoG, reflect when reaching the Moroccan slope.

We used the compressible Coastal and Regional Ocean COmmunity (CROCO) solver with a 10 m resolution horizontal grid and 200 sigma levels. The full description is provided in Hilt et al. (2020) who analyzed the I-waves generation at CS. Here, we initialize the stratification with an analytical profile which fits the density profile observed at MO5 after the I-waves detection the 15 October (see inset in Figure 8a). This method resembles sigmoid density profile used to model the stratification in the SoG in some previous papers (Echevarría et al., 2002; Vargas et al., 2006). The incident wave is initialized in amplitude and horizontal speed with a solution of the Dubreuil-Jacobi-Long equations (Dunphy et al., 2011; Turkington et al., 1991) for this stratification with different amplitudes 72 m (SimR), 100 m (SimD), and 30 m (SimS) in order to test the sensitivity of the result to the I-waves amplitude. Finally a realistic 50 m resolution topography extracted from the SHOM (Service Hydrographique et Océanographique de la Marine) database is used for the easternmost 20 km of the 30 km long domain. The topography of the first 10 km, where the I-wave is initialized, is flat with the depth of the MO5 mooring. The initial configuration of the three simulations is depicted in Figure 8. The full setup is described in
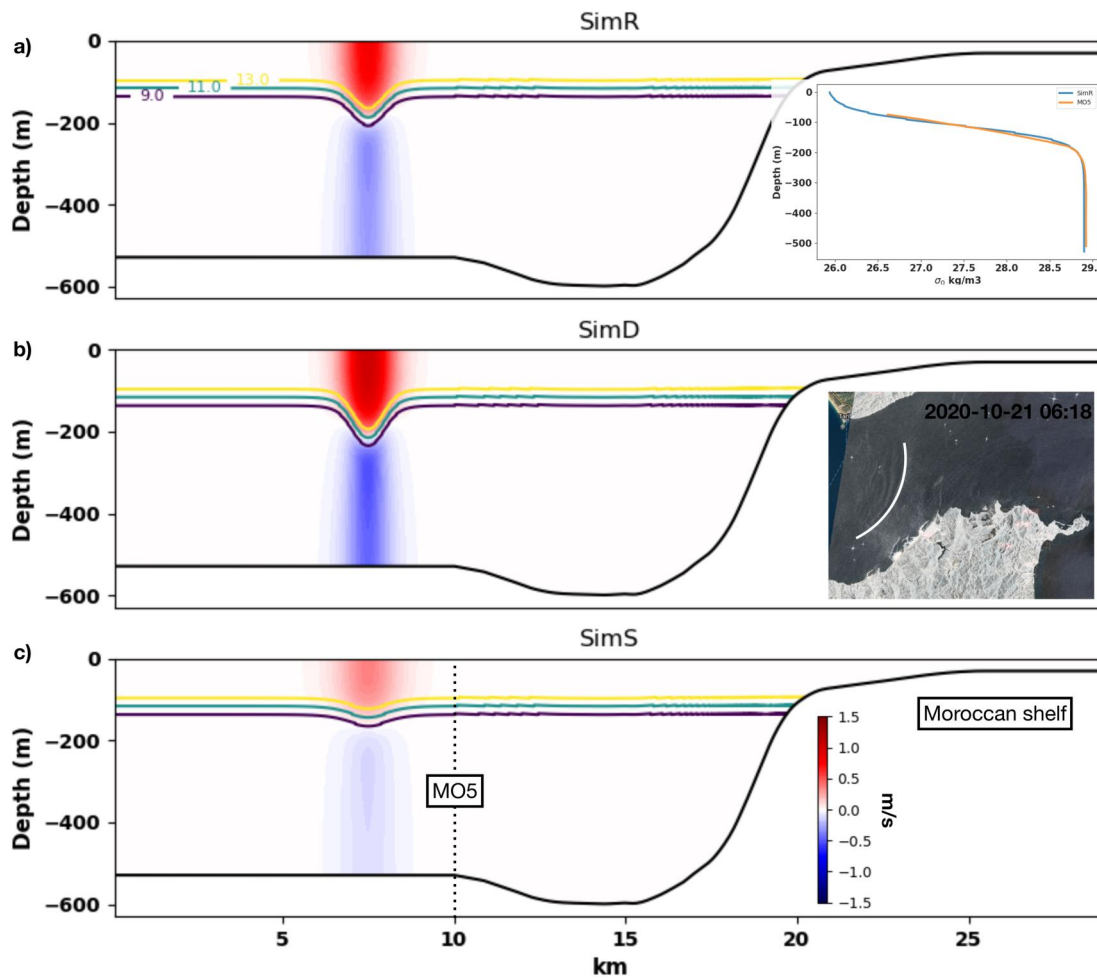
Figure 8. Description of the initialization stage for (a) SimR, (b) SimD, and (c) SimS. Isothermal 9, 11, and 13 are plotted superimposed to the zonal velocity field (color scale). Note that temperature is the only tracer activated for these simulations supporting the stratification. Inset in panel (a) shows the initial stratification profile of the model (blue line) and the time-averaged profile observed at MO5 mooring (orange line) after the observations of I-waves on 15 October. Inset in panel (b) shows the Sentinel-1 Synthetic Aperture Radar image of 21 October. The approximate location of MO5 mooring in the model domain is indicated in panel (c).

Table 1. The turbulent closure differs from Hilt et al. (2020) as we used the General Length Scale model in the $K - \epsilon$ version (Marchesiello & Treillou, 2023). The east-west boundaries are open forced with the initial stratification with a sponge layer to avoid spurious reflections.

5.2. Reflected ISW

Figures 9–11 show the breaking and reflection of an incident wave over the shelf for SimR, SimD, and SimS respectively. When the incident wave shoals on the slope, the wave tail steepens (Figure 9b), the polarity changes but the elevation pattern collapses rapidly associated with rapid oscillations of the pynocline and vertical velocity, both features suggesting intense mixing (Figure 9c). The breaking resembles a collapsing situation rather than a surging situation as the tail of the incident ISW does not overpass the its front (Aghsaee et al., 2010; Nakayama et al., 2019). At the back of this breaking, part of the energy is reflected in a wave with soliton like structure (Figures 9c and 9d). In SimR, the reflected wave has an amplitude of 33% (24 m) and a wavelength increased by 10% compare with the incident wave (Figure 9d). The phase speed deduced from panel c–d is about 1.5 m/s. For SimD, the incident wave collapses as well and the reflected wave has an amplitude of 33% (33 m) and a wavelength of the same length compare with the incident ISW (Figure 10d). SimS shows different results: the breaking resembles the collapsing situation but for such a small amplitude incident ISW (30 m) no clear signal of reflected ISW is observed (Figure 11d) but rather a small-amplitude gravity wave. These simulations highlight that the Moroccan shelf topography is favorable for the generation of reflected ISWs. This process is sensitive to

Table 1
*Description of the Numerical Parameters for SimR (Same Are Used for SimD and SimS)*

Numerical parameters	SimR
Number of horizontal point	3,000
Horizontal scale Δx	10 m
Number of vertical σ-levels	200
Slow time scale	1/10 s
Fast time scale	1/350 s
Vertical viscosity	10^{-9} m^2/s
Lateral viscosity	0 m^2/s
Diffusivity	0 m^2/s
Momentum Advective Scheme	WENO5
Turbulent Closure Scheme	Generic Length Scale $K - \epsilon$
T advective scheme	WENO5
Bottom drag coefficient C_{drag}	0
Atmospheric forcing/fluxes	None
Boundaries	Open boundaries with sponge layer
Pynocline depth z_{ref}	110 m
Pynocline width Δz	30 m
Density difference Δ_ρ	3 kg/m^3
Stratification	$1,028\left(1 - \frac{\Delta_\rho}{2}\tanh\left[(z - z_{ref})/\Delta z\right]/1,028\right)$

the amplitude of the incident wave, but in the range of the typical I-waves observed in spring tides in the SoG (amplitude between these of SimR and SimD) an ISW is clearly reflected when the incident ISW shoals and breaks.

In SimR, the amplitude of the reflected ISW is reduced by 67%. A careful inspection of the R-waves depicted in Figure 4 shows that the wave amplitude is about 60 m while the corresponding I-waves is 80 m (considering the 1,028 kg/m^3 isopycnal as a reference). Thus the amplitude reduction is of 25% considerably less than for the modeled reflected wave. In addition, these R-waves have a wavelength of 3,240 m, about 3 times longer than I-waves. In SimR, the reflected wave is 10% longer than the incident wave. These results are obviously more simple than reality but the model produces reflected waves weaker and longer than the incident wave. Different reasons might explain the differences between the model and reality: one is the change of pycnocline depth under internal tide effect which is not modeled by this approach. For the same amount of available potential energy, an ISW which propagates in a deeper pycnocline is larger. Indeed, the KdV equation gives a wavelength λ of:

$$\lambda = \frac{2h(H - h)}{\sqrt{3a(2h - H)}} \tag{2}$$

with H the total depth, h the pynocline depth and a the wave amplitude. Thus a change of h from 100 to 200 m (representative depth of the R-waves observed in Figure 5) retaining the same amplitude for the ISW the wavelength increases by a factor 2.6, consistent with the observations.
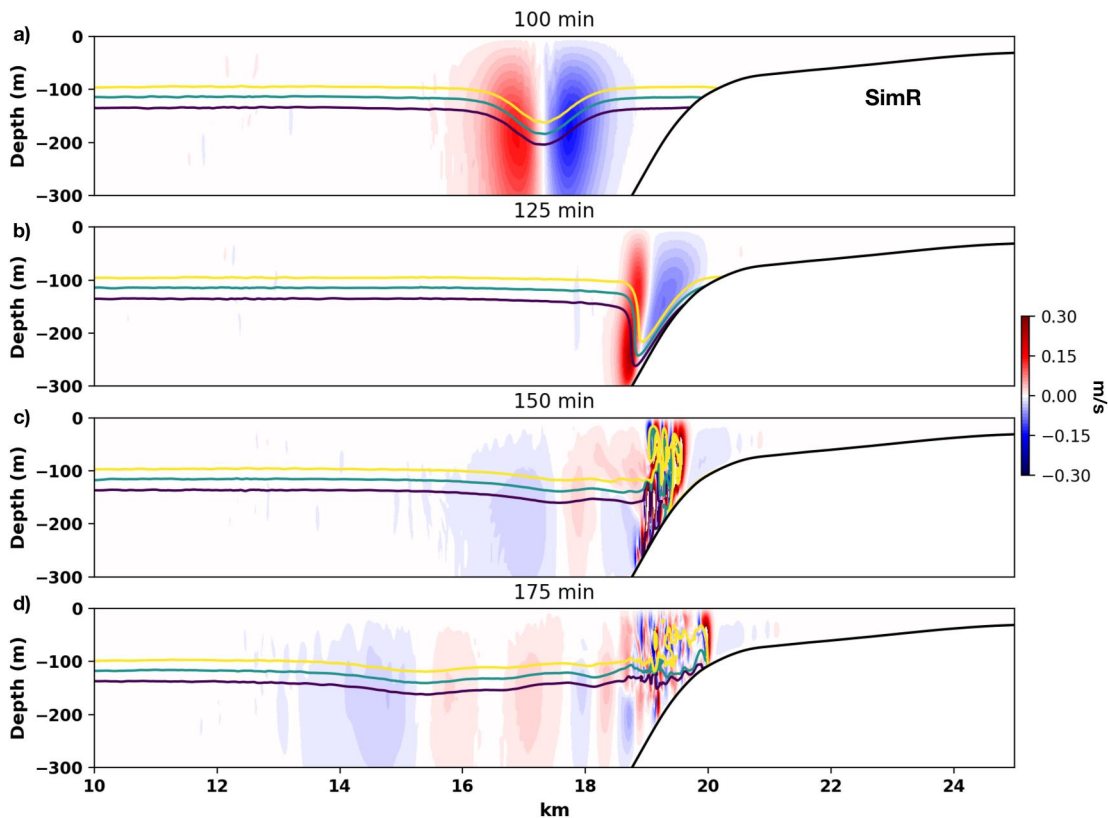
Figure 9. Vertical velocity superimposed with 9, 11, and 13 isothermals at different stages of the simulation for SimR.
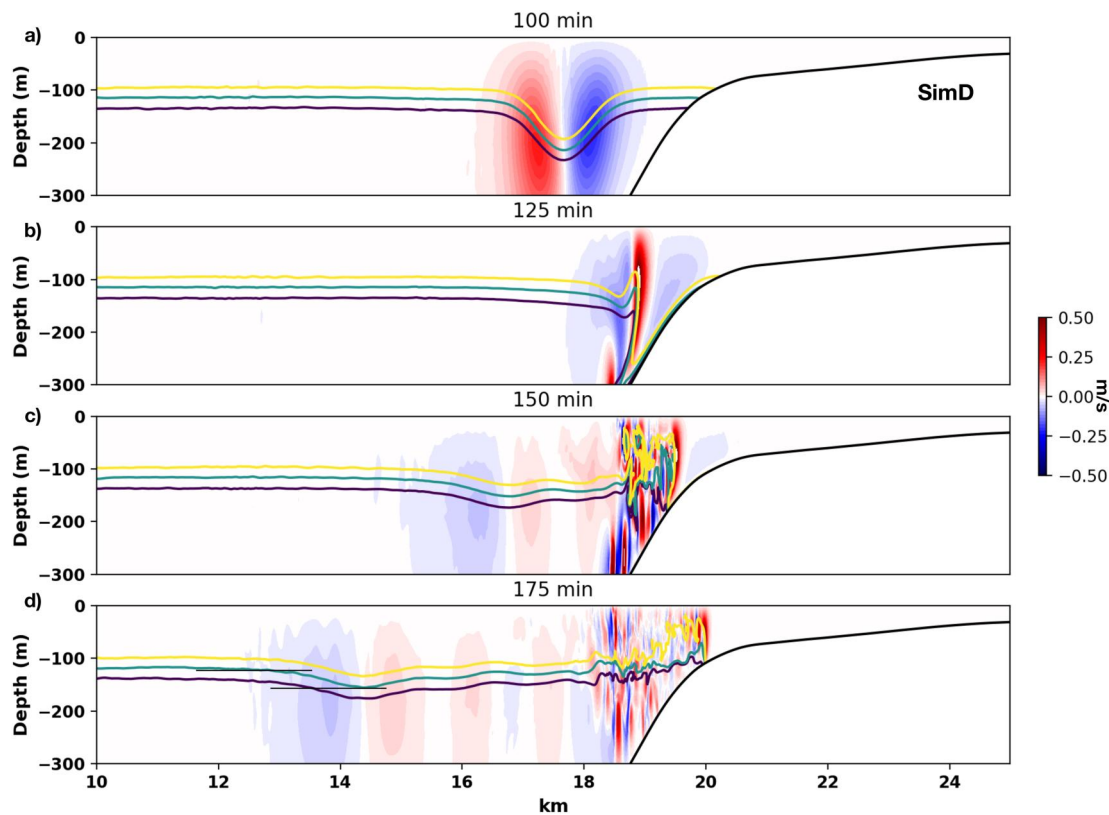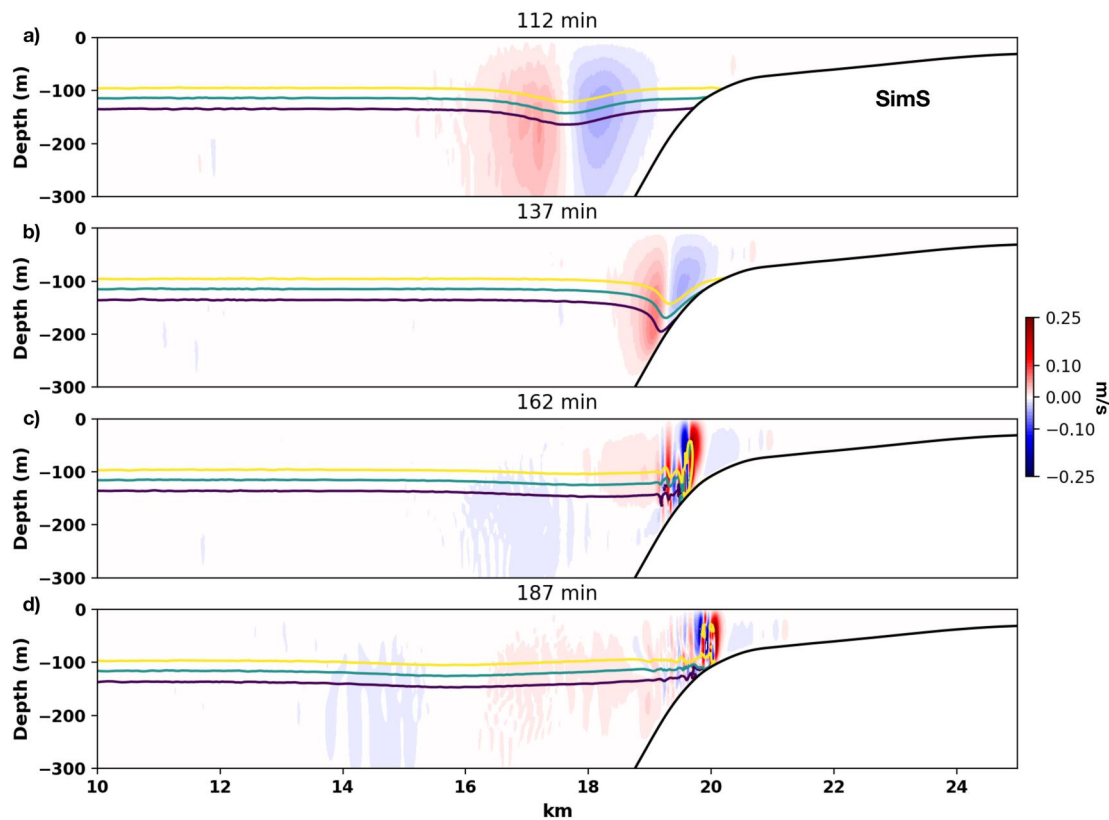
Figure 10. Vertical velocity superimposed with 9, 11, and 13 isothermals at different stages of the simulation for SimD.

A complete and fully realistic model of R-waves was not the objective of this simple numerical experiment. The I-waves do not exactly propagate from MO5 toward the coast but much to the east. However, a few satellite images show a tilt of the I-waves front toward the south (e.g., on 21 October 2020 inset of Figures 2b and 8b). Thus, the wave can be expected to reach the Moroccan shelf perpendicular to isobaths. Another point is that I-waves are 3D; thus this simple model does not include lateral and Coriolis effects. But the latter is not the dominant process in the ISW energy transfer in the SoG (Vlasenko et al., 2009). Our numerical approach takes no account of either long-term baroclinic exchange and tidal currents, which slightly impact ISW properties. The modulation of the pycnocline depth under internal tide effect is not modeled. Finally, we initialize only one incident solitary waves while a train is observed, which might explain the differences in the wave amplitude between R-waves and modeled reflected waves. Despite this fact, our numerical approach reveals that under the stratification conditions of the PROTEVS GIB20 field experiment, ISWs with amplitude observed in the SoG can reflect when shoaling and breaking along the Moroccan shelf.

We performed additional tests, especially to check the sensitivity of the result to the depth of the pycnocline. Indeed, as previously mentioned the depth of the pycnocline is displaced by the internal tide in the SoG (Morozov et al., 2002). The other point is the slight meridional tilt of the pycnocline due to Coriolis acceleration (Bray et al., 1995; Naranjo et al., 2015). These two points make the estimation of the real pycnocline depth when the incident waves reaches the shelf quite uncertain. We run SimR for two other pynocline depths $z_{ref} = 80$ m and $z_{ref} = 140$ m. It does not change the main result that a reflected ISW is created when the incident ISW reaches the shelfbreak. The properties of the reflected wave in each case are summarized in Table 2. Note that we also checked the impact of the bottom stress which had been set to zero in SimR. It reveals very similar result for the amplitude of the reflected wave.

5.3. Sea Level Anomaly

As the compressible CROCO model has a free-surface solver, we investigate the behavior of the sea-level anomaly when an incident ISW breaks along the slope. We aim to confirm that a sea-surface signature can

Figure 11. Vertical velocity superimposed with 9, 11, and 13 isothermals at different stages of the simulation for SimS.

propagate toward the coast even when the ISW has broken. Figure 12b presents a Hovmöller diagram of the sea surface displacement ζ for SimR. In the first 120 min, it depicts a 10 cm positive anomaly associated with the incident depression ISW. After 125 min, when the incident wave starts shoaling (Figures 9b), three distinguishable rays appear, a 4 cm elevation propagating eastward which signals the reflected ISWs, an evanescent 2 cm depression anomaly, which corresponds to the breaking elevation ISW formed in the shoaling process. Finally, another elevation signature of about 8 cm propagates much more quickly from the shoaling point to the coast. The phased speed of this signature is about 25 m/s, what corresponds to the phase speed of a surface gravity wave at 60 m depth, consistent with the averaged depth from the shoaling zone to the coast. Thus, this signature is probably associated with a surface gravity wave, generated by the shoaling of the incident ISW on the shelf. Figure 12b presents the high-frequency sea level oscillation, ζ_{HF} at two points of the domain, one far from the slope (orange curve) the other on the shelf near the coast (blue curve). It confirms the signature of the incident ISW near the coast with a typical oscillation of 2 cm (half the amplitude of the incident ISW far from the slope). The period of this signature (about 25 min) is slightly similar to the period of the incident ISW sea level signature.

The model presented here does not represent the shelf topography of the Spanish coast near Tarifa. Thus we can not directly link this result with the surface signature observed in the Tarifa high-frequency sea level oscillations.

Table 2
Sensitivity Tests to Pycnocline Depth and Bottom Drag

Parameter which vary from SimR	Reflected amplitude (% of incident wave) (%)	Wavelength (% of incident wave) (%)	Breaking type
NONE	33	110	Collapsing
$z_{ref} = 140$ m	46	108	Collapsing
$z_{ref} = 80$ m	25	95	Collapsing
$C_{drag} = 2$ mm	38	100	Collapsing

Note. Notations refer to the one used in Table 1.
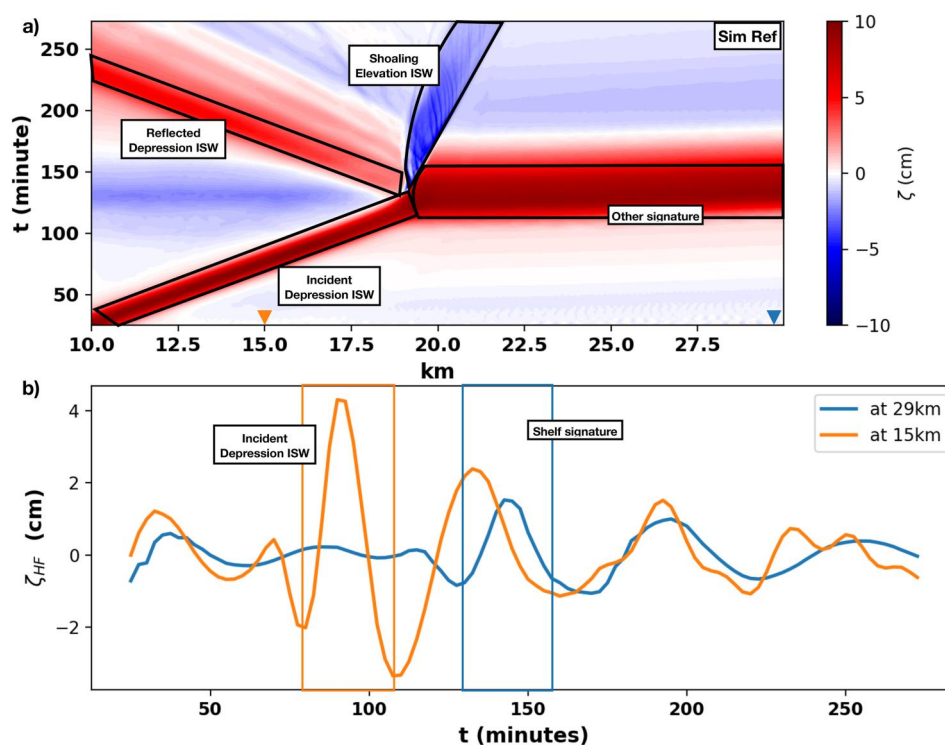
Figure 12. (a) Hovmöller diagram of the sea surface elevation ζ (cm). Black boxes illustrate the different wave signatures. (b) High frequency (eighth order high-pass Butterworth filter at 1cph) of the sea level elevation ζ at two points: 15 km (orange curve), 29 km (blue curve). The location of the selected points are indicated in panel (a) with colored inverted triangles.

However, our simple numerical model suggests a mechanism that transfers the energy from the baroclinic ISW to the barotropic sea surface elevation when the ISWs break. In addition, the high-frequency sea level signature is about 2 cm, which is the order of magnitude observed with the Tarifa tide gauge. At least, it confirms the possibility to observe a remanent signature of ISWs in sea level signal at the coast. The similarity in the signal period of the incident ISW and shelf high-frequency sea level signature matches well with our observation between the Tarifa tide gauge and MO4 mooring, where both signatures have 30 min duration.

6. Discussion

The analysis of SAR and optical images reveals a front tilted to the northwest regardless of the time of the year. ISWs have long been shown to have a clear signature in radar images due to the change in the surface roughness induced by surface convergence/divergence of the velocity field (Alpers et al., 1996; Gomez-Enri et al., 2007; Richez, 1994; Watson & Robinson, 1990). The signatures reported here are typical of ISWs in the SoG (Gomez-Enri et al., 2007; Jackson & Apel, 2004). However, the front tilt is different from the one associated to eastward propagating I-waves. Even more, the extensive review of the ISWs in the SoG (Jackson & Apel, 2004), reports wave patterns different from this one in all cases. Apart from the well-known I-waves, Watson and Robinson (1990) reported northward propagating waves using shore-based radar observations and Brandt et al. (1996) discussed westward propagating ISW west of CS. The first wave pattern was detected at the eastern exit of the SoG heading toward Algeciras Bay (see Figure 2a). The last ones appeared west of CS (Figure 14 of Jackson & Apel, 2004) and were attributed to disturbances of the seasonal thermocline rather than of the halocline (Brandt et al., 1996). In addition, the shape of these westward propagating ISWs is quite different from the R-waves reported here. Their front is clearly north-south without a northward component in the wavenumber. The R-waves discussed here are observed in all seasons, winter included when the seasonal thermocline does not exist. Thus both the season-independent appearance and the location in the SoG east of CS confirm that the reported waves have a totally different origin from the westward or northward waves reported in the literature.

In-situ measurements allowed to detect internal wave signatures both in current and hydrology at the end of each ebb during spring tides, at least whenever an I-wave packet is detected at the beginning of the ebb (Figure 3d). The comparison of the times of arrival at the two moorings and the signature of the meridional baroclinic current evidence the northwestward propagation of the R-wave front. Unfortunately, satellite observations of R-waves were not available at the time of the in-situ measurements. We assume, however, that the R-waves observed with moorings measurements and the satellite observations reported in this study are waves with the same physical origin as they arrive at the same tidal phase at Tarifa and propagate in the same direction.

Watson and Robinson (1990) considered different origins for the northward propagating waves they observed in the eastern part of the SoG: reflection of the eastward going waves (I-waves) at the southern slope of the SoG, disturbances of the northern edge of the Atlantic Jet, and shock waves due to prominent bathymetric feature. The authors retained the last hypothesis (shock waves) because of the non-coherent shift between the eastward I-waves and northward waves they observed, thus rejecting reflection as a source. The examination of their findings with the position of the Atlantic Jet during a field experiment (Armi & Farmer, 1988) raises doubts on the second hypothesis. Recently, Bolado-Penagos et al. (2023) confirmed their conclusions. From a numerical 3D model, they highlighted the generation area which corresponds to a promontory east of Ceuta where hydraulic control happens at some stage of the tide. In our case, we show that the R-waves seem phase-locked with the tidal ebb current and arrive almost 5 hr later than the well-known I-waves at the mooring sites MO4/MO5 (Figures 3d and 5). In addition, no R-waves were observed without the concomitant observation of the I-waves at the beginning of the ebb. The slight variability observed in the arrival time at Tarifa (Figure 6b) can be explained by the fact that the waves are not strictly northward but northwestward and are therefore influenced by variations in the strength of the tidal current. The influence appears to be notable on the ISW fronts mapping on Figure 2a. This figure depicts a clear relation between the northward position of the R-waves and eastward position of the I-waves which argues in favor of a relation between these waves. But a variability still exists, which is partly attributable to the tidal current strength which impacts differently the R-waves and I-waves.

These observations suggest that the R-waves observed are due to reflections of the incident I-waves on the shelf of the Moroccan coasts. Our understanding of the reflection of ISWs on slope is scarce; it is essentially based on tank experiments of Boegman et al. (2005), Helfrich (1992), and Michallet and Ivey (1999) for gentle slopes and (Chen et al., 2007) for steeper slopes. All these experiments showed that the mechanism is quite complex and that the steepness of the slope and the soliton amplitude are key aspects of the reflection. They characterized the reflection by the reflectance defined as the ratio between the incident and reflected wave energy. Bourgault and Kelley (2007) attempted to parameterize the reflectance using previous experiments and numerical simulations at the laboratory scale. The authors showed that it is positively correlated with the Iribarren number:

$$\xi = \frac{s}{\sqrt{a_0/L_w}} \tag{3}$$

with s the slope, a_0 the amplitude of the incident soliton and $L_w = \frac{1}{a_0}\int_{x_1}^{x_2}|\eta(x)|\mathrm{d}x$ the width at the depth of the maximum displacement. However, Lamb and Nguyen (2009) showed that such a parametrization is sensitive to the Reynolds' number and thus it should be extrapolated at the ocean scale with cautions. Reflected ISWs have been reported at some place (Bai et al., 2017; Bourgault et al., 2011; Davis et al., 2020; Klymak et al., 2011), but the observations remains too scarce to build an in-situ parametrization.

For example, Bai et al. (2017) studied reflected ISWs in the China Sea using modeling and satellite images. They showed that about 20% of the incident ISWs energy is reflected by the Dongsha Atoll shelf, whose slope is 0.01. These waves have an amplitude of 80 m with a wavelength of $O(1\ \text{km})$. The I-waves in the SoG are comparable with those observed in the China Sea but the slope of the Moroccan shelf is 0.1 (along the profile selected for the numerical modeling Figure 8) which is quite steep. Thus the Iribarren number along the Moroccan shelf should be 10 times higher than at Dongsha Atoll. As a consequence, it is very likely that part of the energy of the I-waves in the SoG is reflected by the Moroccan shelf.

Using a numerical approach, we demonstrated that when ISWs with the typical amplitude observed in the SoG head on toward the Moroccan shelf, a part of the energy is reflected depending on the amplitude of the incident wave. We assume the simplifications involves by this approach, which is widely used to describe the shoaling of ISWs in the literature (Bai et al., 2017; Bourgault & Kelley, 2007; Davis et al., 2020). It aims to investigate the

possibility for ISWs to reflect on the Moroccan coast leading to the R-waves we depicted in this study. It shows that R-waves can be due to the reflection of I-waves on the shelf, but other data near the shelf zone, a two(multi)-layers depth-integrated two-dimensional model or a fully 3D model are necessary to draw final conclusions, as the shoaling of ISWs is probably impacted by the local dynamics and the wave-wave interactions (Davis et al., 2020). As far as we know, the ISW-shelf interaction has been poorly studied in the SoG. The existence of this newly identified R-waves hints to rich and interesting dynamics on the shelfbreak.

A final remark to support the hypothesis of reflected waves concerns the propagation time. Figure 2d shows that while the I-wave has traveled 30 km, the R-wave traveled 26 km, of which 14 km were eastward as incident and 12 km northwestward as reflected. Therefore, while the I-wave propagates over 16 km the R-wave travels 12 km, giving a ratio of 1.33 between the incident/reflected phase speed. This is consistent with eastward tidal advection of the I-wave during the ebb. Note that we took the isobath 200 m for the calculation, suggested to be the breaking depth by the numerical approach. The 5 hr lag between the I-wave and R-wave observed at MO5, can be theoretically estimated based on a KdV approach. Such a computation involves strong hypothesis regarding the amplitude of the ISW, the depth of the interface and the advection by the tidal current during the propagation of each wave. A rough analysis of the delay using the observations of the 15 October yields about 4 hr compared with the observed 5 hr. This is a correct order of magnitude considering all approximations used.

An interesting fact is that the reflected R-waves are only observed heading northward. In a zonal channel without rotation, reflections from the two sides of the channel are expected to occur, giving rise to southward and northward propagating waves. Figure 2a shows that the central part of the Moroccan shelf is oriented toward the northeast, making an angle of about 37° with the zonal direction (Figure 1). This could explain partly the asymmetry of the reflected waves. This effect of the coast orientation is evidenced in the satellite images: we can observe a very good match between the wave front and the Moroccan shelf orientations. On the other hand, Vlasenko et al. (2009) showed that the Coriolis effect is not negligible in the SoG, whose width is comparable to the local internal Rossby radius (about 14 km). Earth rotation favors the transfer of ISW energy from the north to the south of the SoG and increases the potential of I-waves to be partially reflected at the southern shelf since there is more of the energy capable of being reflected.

Another interesting feature of the reported R-waves concerns their polarity. We developed the idea that the R-waves can be either an elevation or a depression depending on the depth of the halocline, which in turn depends on the internal tide variability. If the observed pattern is a depression wave in early spring tide (Figure 5b), it is less clear when the tidal strength increases (Figure 5f). The tidal strength directly impacts the deepening of the interface between the Atlantic and Mediterranean layers through the internal tide oscillation, as observed in Figure 3b. The reversal of the polarity on ISWs has been modeled by Grimshaw et al. (2004) in the frame of the extended KdV equation, and by Vlasenko and Stashchuk (2007) with a fully 3D model. These studies provide information of the behavior of ISWs reaching a critical point as they propagate to a shelf. Shroyer et al. (2009) show the quite good agreement of the KdV critical point with in-situ observation along the New Jersey coast. The authors evidence that a depression solitary wave transforms into a depression tail when reaching the critical point then leading to a tail of elevation waves. Recently, in the northern South China Sea Zhang et al. (2018) reveal that the position of the critical point along the shelf is modulated by the internal tide. Here the situation is slightly different as the moorings are located in deep sea far from the shelf where no polarity inversion is expected. We can use the previous results to assess the possibility of such a reversal in our case. The KdV theory in presence of a background current gives the critical interface as:

$$\frac{h_1}{h_2} = \frac{c_0 - U_1}{c_0 - U_2} \tag{4}$$

with h_1, h_2 the thickness of upper and lower layer respectively, c_0 the phase speed of the wave and U_1, U_2 the current background in each layer in the direction of the wave propagation. Computing the critical depth with the observations of 16 October afternoon gives a value of $h = 260$ m (see Figure 13 and caption there for the velocity values used in Equation 4 when computing the critical depth). This is near the observed interface depth (defined as the depth of the maximum vertical shear of the zonal current), which reaches 248 m depth at the time of the wave observations (Figure 13).

It contrasts with the case of the 14 October when a critical depth of 325 m is obtained from Equation 4 using the velocity conditions recorded this day, which are indicated in the caption of Figure 13. Therefore, the observed
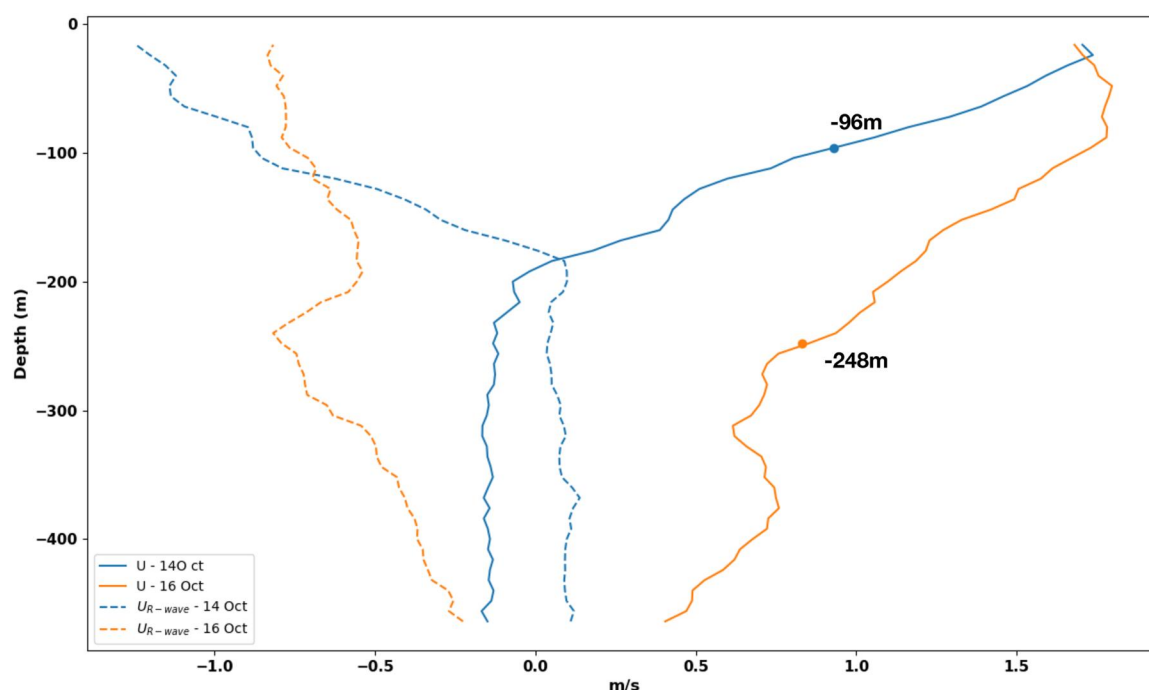
Figure 13. Averaged zonal velocity (full lines) and R-wave direction projected current (dashed lines) in the 15 min preceding the R-wave observation the 14 October (blue) and the 16 October (orange). The scatter points evidence the position of the dynamical interface, defined as the position of the maximum gradient of the zonal current. The averaged values for the upper layer are −1.07 and −0.7 m/s the 14th and 16th respectively. The averaged values for the lower layer are −0.02 and −0.5 m/s the 14th and 16th respectively.

interface is around 100 m (96 m, Figure 13), notably shallower than that critical depth, and no polarity reversal is expected. However, pycnocline depth approaches the critical depth on 16 October, in which case the R-waves might reverse their polarity or, at least, be in the transition phase discussed by Shroyer et al. (2009). The synchronization between the internal tide and the R-waves possibly impacts the polarity of the wave. As far as we know such waves have not been investigated in the 3D fully non linear model of the SoG (Sánchez-Garrido et al., 2011; Sannino et al., 2004). Hilt (2022) briefly evokes R-wave like signatures but it would be interesting to deeply evaluate the capacity of realistic models to reproduce this phenomenon.

The last key point of our study is the signature of the reflected ISWs in the sea level at Tarifa. Satellite images reveal that the front of the reflected waves intercepts Tarifa and our moorings almost at the same time. High-frequency oscillation of the sea level at Tarifa reveals spikes in phase with the R-wave signature in our moorings. The analysis of longer sea level data shows a good correlation between these spikes and the spring tide phased lock around the LW at Tarifa. All these elements allow us to relate the high-frequency peaks observed in the sea level with the R-waves. The physical origin of the sea level high-frequency oscillation would be linked to the sea level perturbation of an ISW (Álvarez et al., 2011; Vlasenko et al., 2009). The latter authors showed a typical signature of a few centimeters on the free surface for waves propagating eastward and decreasing rapidly when they reach the coast, as suggested by our simple numerical model. The order of magnitude is consistent with our observations. Internal solitary waves do not propagate toward the very shallow water where the tide gauge is located (7 m depth in the harbor of Tarifa, see the inset Figure 2b), since the main stratification disappears at this depth. However, the surface signal generated by the wave during it northwestward propagation could persist after its collapse and could propagate toward the coast. The frequency of such a signal with typical period of 30–60 min is far from the frequency spectrum of wind-induced surface gravity waves and might propagate without much interaction to the coastal tide gauge. Even more, Chapman and Giese (1990) highlighted a dynamical mechanism of energy transfer from baroclinic to barotropic mode able to explain the coastal seiche generated by high amplitude internal tide observed in Puerto Rico (Giese et al., 1982, 1990). Our numerical simulation show that the shoaling of ISW on the Moroccan slope leaves effectively a signature in the sea level. A dedicated study should be conducted to understand if this mechanism occurs in the SoG and could be a generating process for the (small) seiche reported in Tarifa harbor (Delgado et al., 2011).

7. Conclusion

Using satellite and in-situ measurements we provided evidence of the existence of northwestward propagating ISWs (R-waves) in the SoG. We provided clues that these waves are due to the reflection of the incident ISWs (I-waves) propagating eastward from CS toward the Alboran Sea. These R-waves, with an amplitude of about 60 m, present a large variability of periods typically ranging from 30 to 60 min. This exhibits some complex signatures in the vertical velocity profile associated which are phase locked with the incident waves. In early spring tide they sign as clear depression solitary waves, while with the increasing tidal strength the pattern is much more complicated with transition-like signature at certain times. Complexification occurs with the deepening of the interface between the Atlantic and Mediterranean layers due to a stronger internal tide. When the halocline reaches the critical point polarity of the R-waves can change. The interaction between internal tide and ISWs deserves a dedicated study to fully understand the possible interaction and consequences on the inertia-gravity wave dynamics. Finally, it is shown that the R-waves have a signature on the high-frequency variations of the sea level at Tarifa. This result is quite new and allows further studies with the long-term time series available at the Tarifa tide gauge. It could also be extended to other geographical sites with similar ISW properties.

The existence of northwestward propagating wave suspected to be reflected waves certainly involved breaking of the eastward propagating ISWs along the Moroccan shelf, which impacts the biology and biochemistry of the area. Camarinal Sill has long been described as the mixing hotspot of the SoG and the site of large ISWs generation, but the continental shelf and coastal zone of the SoG remain poorly understood. This paper highlights the need to increase observation and modeling efforts on the continental shelf and coastal zone of the SoG to better understand and characterize the complex mixing and transport processes that occur there.

Data Availability Statement

- The PROTEVS GIB 20 data used in this paper are available at https://www.seanoe.org/data/00819/93129/ (Bordois & Dumas, 2023).
- The Tarifa tide gauge data are available and downloadable on the web site of Puertos del Estado (Spain): http://opendap.puertos.es/thredds/catalog.html (Puertos del Estado (Spain), 2023).
- The MATLAB DJLES package Dunphy et al. (2011) used to initialized the ISW in our numerical model is provided as a github package: https://github.com/mdunphy/DJLES (Dunphy et al., 2022).

References

Aghsaee, P., Boegman, L., & Lamb, K. G. (2010). Breaking of shoaling internal solitary waves. *Journal of Fluid Mechanics*, *659*, 289–317. https://doi.org/10.1017/S002211201000248X

Alpers, W., Brandt, P., Rubino, A., & Backhaus, J. (1996). Recent contributions of remote sensing to the study of internal waves in the Straits of Gibraltar and Messina. *Bulletin de l'Institut Oceanographique*, *17*, 21–40.

Álvarez, O., González, C. J., Mañanes, R., López, L., Bruno, M., Izquierdo, A., et al. (2011). Analysis of short-period internal waves using wave-induced surface displacement: A three-dimensional model approach in Algeciras Bay and the Strait of Gibraltar. *Journal of Geophysical Research*, *116*(C12), C12033. https://doi.org/10.1029/2011JC007393

Armi, L., & Farmer, D. (1985). The internal hydraulics of the Strait of Gibraltar and associated sills and narrows. *Oceanologica Acta*, *8*(1), 37–46.

Armi, L., & Farmer, D. (1988). The flow of Atlantic Water through the Strait of Gibraltar. The flow of Mediterranean Water through the Strait of Gibraltar. *Progress in Oceanography*, *21*, 1–105.

Bai, X., Li, X., Lamb, K. G., & Hu, J. (2017). Internal solitary wave reflection near Dongsha Atoll, the South China Sea. *Journal of Geophysical Research: Oceans*, *122*(10), 7978–7991. https://doi.org/10.1002/2017JC012880

Boegman, L., Ivey, G., & Imberger, J. (2005). The degeneration of internal waves in lakes with sloping topography. *Limnology & Oceanography*, *50*(5), 1620–1637. https://doi.org/10.4319/lo.2005.50.5.1620

Bolado-Penagos, M., Sala, I., Jesús Gomiz-Pascual, J., González, C. J., Izquierdo, A., Álvarez, Ó., et al. (2023). Analysis of internal soliton signals and their eastward propagation in the Alboran Sea: Exploring the effect of subinertial forcing and fortnightly variability. *Progress in Oceanography*, *217*, 103077. https://doi.org/10.1016/j.pocean.2023.103077

Bordois, L., & Dumas, F. (2023). protevs gib20 - Camarinal sill [Dataset]. https://doi.org/10.17882/93129

Bourgault, D., Janes, D. C., & Galbraith, P. S. (2011). Observations of a large-amplitude internal wave train and its reflection off a steep slope. *Journal of Physical Oceanography*, *41*(3), 586–600. https://doi.org/10.1175/2010JPO4464.1

Bourgault, D., & Kelley, D. E. (2007). On the reflectance of uniform slopes for normally incident interfacial solitary waves. *Journal of Physical Oceanography*, *37*(5), 1156–1162. https://doi.org/10.1175/JPO3059.1

Brandt, P., Alpers, W., & Backhaus, J. (1996). Study of the generation and propagation of internal waves in the Strait of Gibraltar using a numerical model and synthetic aperture radar images of the European ERS 1 satellite. *Journal of Geophysical Research*, *101*(C6), 14237–14252. https://doi.org/10.1029/96JC00540

Bray, N. A., Ochoa, J., & Kinder, T. (1995). The role of the interface in exchange through the Strait of Gibraltar. *Journal of Geophysical Research*, *100*(C6), 10755–10776. https://doi.org/10.1029/95jc00381

Bruno, M., Alonso, J. J., Cózar, A., Vidal, J., navate, A. R.-C., Echevarría, F., & Ruiz, J. (2002). The boiling-water phenomena at Camarinal Sill, the Strait of Gibraltar. *Deep-Sea Research II*, *49*(19), 4097–4113. https://doi.org/10.1016/s0967-0645(02)00144-3

Bryden, H. L., Candela, J., & Kinder, T. H. (1994). Exchange through the Strait of Gibraltar. *Progress in Oceanography*, *33*(3), 201–248. https://doi.org/10.1016/0079-6611(94)90028-0

Candela, J., Winant, C. D., & Ruiz, A. (1990). Tides the Strait of Gibraltar. *Journal of Geophysical Research*, *95*(C5), 7313–7335. https://doi.org/10.1029/jc095ic05p07313

Chapman, D. C., & Giese, G. S. (1990). A model for the generation of coastal seiches by deep-sea internal waves. *Journal of Physical Oceanography*, *20*(9), 1459–1467. https://doi.org/10.1175/1520-0485(1990)020⟨1459:AMFTGO⟩2.0.CO;2

Chen, C.-Y., Hsu, J. R.-C., Chen, H.-H., Kuo, C.-F., & Cheng, M.-H. (2007). Laboratory observations on internal solitary wave evolution on steep and inverse uniform slopes. *Ocean Engineering*, *34*(1), 157–170. https://doi.org/10.1016/j.oceaneng.2005.11.019

Chioua, J., Bruno, M., Vázquez, A., Reyes, M., Gomiz, J., Mañanes, R., et al. (2013). Internal waves in the Strait of Gibraltar and their role in the vertical mixing processes within the Bay of Algeciras. Estuarine. *Coastal and Shelf Science*, *126*, 70–86. https://doi.org/10.1016/j.ecss.2013.04.010

Davis, K. A., Arthur, R. S., Reid, E. C., Rogers, J. S., Fringer, O. B., DeCarlo, T. M., & Cohen, A. L. (2020). Fate of internal waves on a shallow shelf. *Journal of Geophysical Research: Oceans*, *125*(5), e2019JC015377. https://doi.org/10.1029/2019JC015377

Delgado, J., García-Lafuente, J., Bruque-Pozas, E., & Naranjo, C. (2011). Short period sea level oscillations at Strait of Gibraltar: Observations versus model results. *Estuarine, Coastal and Shelf Science*, *95*(2), 307–313. https://doi.org/10.1016/j.ecss.2011.09.014

Dessert, M., Honnorat, M., Le Caillec, J.-M., Messager, C., & Carton, X. (2022). Estimating the pycnocline depth from the SAR signature of internal waves in the Alboran Sea. *IEEE Journal of Selected Topics in Applied Earth Observations and Remote Sensing*, *15*, 9048–9061. https://doi.org/10.1109/JSTARS.2022.3214298

Dunphy, M., Subich, C., & Stastna, M. (2011). Spectral methods for internal waves: Indistinguishable density profiles and double-humped solitary waves. *Nonlinear Processes in Geophysics*, *18*(3), 351–358. https://doi.org/10.5194/npg-18-351-2011

Dunphy, M., Subich, C., & Stastna, M. (2022). Djles matlab package [Software]. Retrieved from https://github.com/mdunphy/DJLES

Echevarría, F., García Lafuente, J., Bruno, M., Gorsky, G., Goutx, M., González, N., et al. (2002). Physical–biological coupling in the Strait of Gibraltar. *Deep-Sea Research Part II: Topical Studies in Oceanography*, *49*(19), 4115–4130. (Canary Islands, Azores, Gibraltar Observations (Canigo) Volume II: Studies of the Azores and Gibraltar regions). https://doi.org/10.1016/S0967-0645(02)00145-5

García-Lafuente, J., Almazán, J., Castillejo, F., Khribeche, A., & Hakimi, A. (1990). Sea level in the Strait of Gibraltar: Tides. *International Hydrographic Review*, *LXVII*(1), 111–130.

García-Lafuente, J., Sammartino, S., Sánchez-Garrido, J. C., & Naranjo, C. (2018). Asymmetric baroclinic response to tidal forcing along the main sill of the Strait of Gibraltar inferred from mooring observations. In *The ocean in motion* (pp. 193–210). Spinger.

García-Lafuente, J., Vargas, J. M., Plaza, F., Sarhan, T., Candela, J., & Bascheck, B. (2000). Tide at the eastern section of the Strait of Gibraltar. *Journal of Geophysical Research*, *105*(C6), 14197–14213. https://doi.org/10.1029/2000JC900007

Gerkema, T., & Zimmerman, J. (2008). An introduction to internal waves. *Lecture Notes, Royal NIOZ, Texel*, *207*, 207.

Giese, G. S., Chapman, D. C., Black, P. G., & Fornshell, J. A. (1990). Causation of large-amplitude coastal seiches on the Caribbean coast of Puerto Rico. *Journal of Physical Oceanography*, *20*(9), 1449–1458. https://doi.org/10.1175/1520-0485(1990)020⟨1449:COLACS⟩2.0.CO;2

Giese, G. S., Hollander, R. B., Fancher, J. E., & Giese, B. S. (1982). Evidence of coastal seiche excitation by tide-generated internal solitary waves. *Geophysical Research Letters*, *9*(12), 1305–1308. https://doi.org/10.1029/GL009i012p01305

Gomez-Enri, J., Enri, J., Vázquez, A., Bruno, M., & Mariscal, L. (2007). *Characterization of internal waves in the Strait of Gibraltar, using SAR and in-situ measurements*. European Space Agency, (Special Publication) ESA SP.

Gonzalez, N., Waldman, R., Sannino, G., Giordani, H., & Somot, S. (2023). Understanding tidal mixing at the Strait of Gibraltar: A high-resolution model approach. *Progress in Oceanography*, *212*, 102980. https://doi.org/10.1016/j.pocean.2023.102980

Grimshaw, R., Pelinovsky, E., Talipova, T., & Kurkin, A. (2004). Simulation of the transformation of internal solitary waves on oceanic shelves. *Journal of Physical Oceanography*, *34*(12), 2774–2791. https://doi.org/10.1175/JPO2652.1

Helfrich, K. R. (1992). Internal solitary wave breaking and run-up on a uniform slope. *Journal of Fluid Mechanics*, *243*(1), 133–154. https://doi.org/10.1017/S0022112092002660

Hilt, M. (2022). Exploration des fines échelles océaniques dans le détroit de Gibraltar: Simulation numérique, observation et mélange induit.

Hilt, M., Auclair, F., Benshila, R., Bordois, L., Capet, X., Debreu, L., et al. (2020). Numerical modelling of hydraulic control, solitary waves and primary instabilities in the Strait of Gibraltar. *Ocean Modelling*, *151*, 101642. https://doi.org/10.1016/j.ocemod.2020.101642

Jackson, C., & Apel, J. (2004). *An atlas of oceanic internal solitary waves - Strait of Gibraltar* (2nd ed., pp. 179–186). Global Ocean Associate.

Jeans, D. R., & Sherwin, T. J. (2001). The evolution and energetics of large amplitude nonlinear internal waves on the Portuguese shelf. *Journal of Marine Research*, *59*(3), 327–353. https://doi.org/10.1357/002224001762842235

Klymak, J. M., Alford, M. H., Pinkel, R., Lien, R.-C., Yang, Y. J., & Tang, T.-Y. (2011). The breaking and scattering of the internal tide on a continental slope. *Journal of Physical Oceanography*, *41*(5), 926–945. https://doi.org/10.1175/2010JPO4500.1

Kurkina, O., Rouvinskaya, E., Kurkin, A., Giniyatullin, A., & Pelinovsky, E. (2018). Vertical structure of the velocity field induced by mode-I and mode-II solitary waves in a stratified fluid. *The European Physical Journal E*, *41*(3), 47. https://doi.org/10.1140/epje/i2018-11654-3

Lacombe, H., & Richez, C. (1982). The regime of the Strait of Gibraltar. *Hydrodynamics of Semi-Enclosed Seas*, *34*, 13–73. https://doi.org/10.1016/S0422-9894(08)71237-6

Lamb, K. G. (2014). Internal wave breaking and dissipation mechanisms on the continental slope/shelf. *Annual Review of Fluid Mechanics*, *46*(1), 231–254. https://doi.org/10.1146/annurev-fluid-011212-140701

Lamb, K. G., & Nguyen, V. T. (2009). Calculating energy flux in internal solitary waves with an application to reflectance. *Journal of Physical Oceanography*, *39*(3), 559–580. https://doi.org/10.1175/2008JPO3882.1

Laurent, L. S., Simmons, H., Tang, T. Y., & Wang, Y. (2011). Turbulent properties of internal waves in the South China Sea. *Oceanography*, *24*(4), 78–87. https://doi.org/10.5670/oceanog.2011.96

Marchesiello, P., & Treillou, S. (2023). Correction of GLS turbulence closure for wave-resolving models with stratification. *Ocean Modelling*, *184*, 102212. https://doi.org/10.1016/j.ocemod.2023.102212

Michallet, H., & Ivey, G. N. (1999). Experiments on mixing due to internal solitary waves breaking on uniform slopes. *Journal of Geophysical Research*, *104*(C6), 13467–13477. https://doi.org/10.1029/1999JC900037

Morozov, E. G., Trulsen, K., Velarde, M. G., & Vlasenko, V. I. (2002). Internal tides in the Strait of Gibraltar. *Journal of Physical Oceanography*, *32*(11), 3193–3206. https://doi.org/10.1175/1520-0485(2002)032<3193:ititso>2.0.co;2

Nakayama, K., Sato, T., Shimizu, K., & Boegman, L. (2019). Classification of internal solitary wave breaking over a slope. *Physical Review Fluids*, *4*(1), 014801. https://doi.org/10.1103/PhysRevFluids.4.014801

Naranjo, C., Sammartino, S., García-Lajuente, J., Bellanco, M. J., & Taupier-Letage, I. (2015). Mediterranean waters along and across the Strait of Gibraltar, characterization and zonal modification. *Deep-Sea Research I*, *105*, 41–52. https://doi.org/10.1016/j.dsr.2015.08.003

Puertos del Estado (Spain). (2023). Tarifa tide gauge [Dataset]. Retrieved from http://opendap.puertos.es/thredds/catalog.html

Richez, C. (1994). Airbone synthetic aperture radar tracking of internal waves in the Strait of Gibraltar. *Progress in Oceanography*, *33*(2), 93–159. https://doi.org/10.1016/0079-6611(94)90023-x

Roustan, J.-B., Bordois, L., Dumas, F., Auclair, F., & Carton, X. (2023). In situ observations of the small-scale dynamics at Camarinal Sill—Strait of Gibraltar. *Journal of Geophysical Research: Oceans*, *128*(10), e2023JC019738. https://doi.org/10.1029/2023JC019738

Sánchez-Garrido, J. C., Garcia-Lafuente, J., Aldeanueva, F. C., Baquerizo, A., & Sannino, G. (2008). Time-spatial variability observed in velocity of propagation of the internal bore in the Strait of Gibraltar. *Journal of Geophysical Research*, *113*(C7), C07034. https://doi.org/10.1029/2007jc004624

Sánchez-Garrido, J. C., & Nadal, I. (2022). The Alboran Sea circulation and its biological response: A review. *Frontiers in Marine Science*, *9*, 933390. https://doi.org/10.3389/fmars.2022.933390

Sánchez-Garrido, J. C., Sannino, G., Liberti, L., García-Lafuente, J., & Pratt, L. (2011). Numerical modeling of three-dimensional stratified tidal flow over Camarinal Sill, Strait of Gibraltar. *Journal of Geophysical Research*, *116*(C12), C12026. https://doi.org/10.1029/2011jc007093

Sannino, G., Bargagli, A., & Artale, V. (2004). Numerical modeling of the semidiurnal tidal exchange through the Strait of Gibraltar. *Journal of Geophysical Research*, *109*(C5), C05011. https://doi.org/10.1029/2003JC002057

Shroyer, E., Moum, J., & Nash, J. (2009). Observation of polarity reversal in shoaling nonlinear internal waves. *Journal of Physical Oceanography*, *39*(3), 691–701. https://doi.org/10.1175/2008jpo3953.1

Turkington, B., Eydeland, A., & Wang, S. (1991). A computational method for solitary internal waves in a continuously stratified flow. *Studies in Applied Mathematics*, *85*(2), 93–127. https://doi.org/10.1002/sapm199185293

Vargas, J., Lafuente, J. G., Candela, J., & Sánchez, A. J. (2006). Fortnightly and monthly variability of the exchange through the Strait of Gibraltar. *Progress in Oceanography*, *70*(2–4), 466–485. https://doi.org/10.1016/j.pocean.2006.07.001

Vázquez, A., Bruno, M., Izquierdo, A., Macías, D., & Cañavate, A. R. (2008). Meteorologically forced subinertial flows and internal wave generation at the main sill of the Strait of Gibraltar. *Deep-Sea Research I*, *55*(10), 1277–1283. https://doi.org/10.1016/j.dsr.2008.05.008

Vázquez, A., Flecha, S., Bruno, M., Macías, D., & Navarro, G. (2009). Internal waves and short-scale distribution patterns of chlorophyll in the Strait of Gibraltar and Alborán Sea. *Geophysical Research Letters*, *36*(23), L23601. https://doi.org/10.1029/2009GL040959

Vlasenko, V., Garrido, J. C. S., Stashchuk, N., Garcia-Lafuente, J., & Losada, M. (2009). Three-dimensional evolution of large-amplitude internal waves in the Strait of Gibraltar. *Journal of Physical Oceanography*, *39*(9), 2230–2246. https://doi.org/10.1175/2009JPO4007.1

Vlasenko, V., & Stashchuck, N. (2007). Three-dimensional shoaling of large-amplitude internal waves. *Journal of Geophysical Research*, *112*(C11), C11018. https://doi.org/10.1029/2007jc004107

Watson, G., & Robinson, I. (1990). A study of internal wave propagation in the Strait of Gibraltar using shore-based marine radar images. *Journal of Physical Oceanography*, *20*(3), 374–395. https://doi.org/10.1175/1520-0485(1990)020<0374:asoiwp>2.0.co;2

Wesson, J. C., & Gregg, M. (1994). Mixing at Camarinall Sill in the Strait of Gibraltar. *Journal of Geophysical Research*, *99*(C5), 9847–9878. https://doi.org/10.1029/94jc00256

Zhang, X., Huang, X., Zhang, Z., Zhou, C., Tian, J., & Zhao, W. (2018). Polarity variations of internal solitary waves over the continental shelf of the northern South China Sea: Impacts of seasonal stratification, mesoscale eddies, and internal tides. *Journal of Physical Oceanography*, *48*(6), 1349–1365. https://doi.org/10.1175/JPO-D-17-0069.1

Ziegenbein, J. (1969). Short internal waves in the Strait of Gibraltar. *Deep-Sea Research*, *16*(5), 479–487. https://doi.org/10.1016/0011-7471(69)90036-9

Ziegenbein, J. (1970). Spatial observations of short internal waves in the Strait of Gibraltar. *Deep-Sea Research*, *17*(5), 867–875. https://doi.org/10.1016/0011-7471(70)90004-5